AGU PUBLICATIONS

JGR

Journal of Geophysical Research: Solid Earth

RESEARCH ARTICLE
10.1002/2016JB013486

Key Points:
- The asthenospheric mantle beneath the eastern NCC is stratified
- Lithospheric thinning/thickening of the eastern NCC induced shift of magma source
- The low-velocity mantle domains beneath the eastern NCC are related to metasomatism by carbonatite

Supporting Information:
- Supporting Information S1

Correspondence to:
H.-Y. Li,
hongyanli@gig.ac.cn

Citation:
Li, H.-Y., Y.-G. Xu, J. G. Ryan, and S. A. Whattam (2017), Evolution of the mantle beneath the eastern North China Craton during the Cenozoic: Linking geochemical and geophysical observations, *J. Geophys. Res. Solid Earth*, *122*, 224–246, doi:10.1002/2016JB013486.

Received 23 AUG 2016
Accepted 27 DEC 2016
Accepted article online 30 DEC 2016
Published online 21 JAN 2017

Evolution of the mantle beneath the eastern North China Craton during the Cenozoic: Linking geochemical and geophysical observations

Hong-Yan Li[1], Yi-Gang Xu[1], Jeffrey G. Ryan[2], and Scott A. Whattam[3]

[1]State Key Laboratory of Isotope Geochemistry, Guangzhou Institute of Geochemistry, Chinese Academy of Sciences, Guangzhou, China, [2]School of Geosciences, University of South Florida, Tampa, Florida, USA, [3]Department of Earth and Environmental Sciences, Korea University, Seoul, South Korea

Abstract Recent discoveries related to the geochemistry of Cenozoic basalts and the geophysics of the deep mantle beneath eastern Eurasia make it possible to place constraints on the relationship between the seismic tomography of subcontinental mantle domains and their geochemical heterogeneities. Basalts with ocean island basalt-like trace elements erupted during (56–23 Ma) and after (≤23 Ma) rifting of the eastern North China Craton (NCC) show evidence for the mixing of an isotopically depleted source and an EMI (Enriched mantle type I) pyroxenitic mantle. NCC rifting-stage basalts exhibit anomalously low MgO and $Fe_2O_3^T$ and high SiO_2 and Al_2O_3, as well as low Dy/Yb and Y/Yb and high ε_{Hf} at a given ε_{Nd}, as compared to the postrifting basalts. Temporal compositional variations and their association with basin subsidence indicate that heterogeneity in the eastern NCC asthenospheric mantle is the primary driver for intraplate magmatism in this region. The specific magmatic sources shifted in terms of depth, related to lithospheric thinning and thickening in the eastern NCC. The NCC EMI mantle domain most likely developed due to ancient events, is persistent through time, and is not related to dehydration of the stagnant Pacific slab in the mantle transition zone. Based on the chemical signatures of postrifting basalts, contributions from the Pacific slab are likely to be carbonatite rich. Mantle metasomatism by carbonatite melts from the Pacific slab and the interaction of these melts at shallower depths with EMI pyroxenitic mantle domains to trigger melting are contributors to the observed low *P* wave velocity zone beneath eastern Eurasia.

1. Introduction

Recent advances in the geophysical observation of the deep mantle and the geochemistry of intraplate basaltic rocks demonstrate some clear relationships. It has been widely observed geophysically, via *P* wave seismic tomography, that quasi-vertical conduits, imaged as low-velocity zones, extend to the core-mantle boundary beneath many prominent hot spots, including Hawaii, the Canaries, and Iceland [e.g., *Lei and Zhao*, 2006; *French and Romanowicz*, 2015]. These low *P* wave anomalies are commonly interpreted as hot or wet upwelling mantle ± associated melts that feed these volcanic centers. Geochemically, these hot spot lavas are now believed to be dominantly derived from mantle domains enriched in pyroxenite [e.g., *Sobolev et al*., 2005, 2007; *Herzberg*, 2006; *Gurenko et al*., 2009]. In Hawaii, the shield stage Koolau, Kilauea, and Mauna Loa tholeiites are largely derived from a pyroxenitic mantle, while preshield Loihi and postshield Haleakala lavas are consistent with a derivation from an olivine-bearing pyroxenitic mantle [*Herzberg*, 2011] or mixing of melts of pyroxenite and peridotite [*Sobolev et al*., 2005]. Thus, the geophysical structure [e.g., *Lei and Zhao*, 2006] and mineralogical makeup [*Sobolev et al*., 2005; *Herzberg*, 2011] of the Hawaiian plume source are correlated, which means that the presence of melt-able pyroxenitic mantle is at least partly responsible for the tomographic low-velocity zone beneath the Hawaiian hot spot.

The mantle tomography of eastern Eurasia shows a very different shape and structure than is seen beneath typical hot spots. A high-velocity, stagnant segment of the subducted Pacific plate is evident in the *P* and *S* wave tomography of the mantle transition zone (MTZ, 410–660 km) beneath eastern Eurasia, and a low *P* wave velocity zone is apparent at shallower mantle depths (Figure 1) [*Fukao et al*., 1992; *Zhao*, 2004; *Zhao et al*., 2009; *Wei et al*., 2015]. Widespread Cenozoic basaltic eruptions have occurred along the eastern margin of Eurasia (Figure 1) [*Zhou and Armstrong*, 1982; *Fan and Hooper*, 1991; *Xu et al*., 2012a], suggesting some relationship with the subducted Pacific slab in the MTZ. Numerous studies have been conducted exploring the possible links between geophysical and geochemical observations in eastern Eurasia, with some

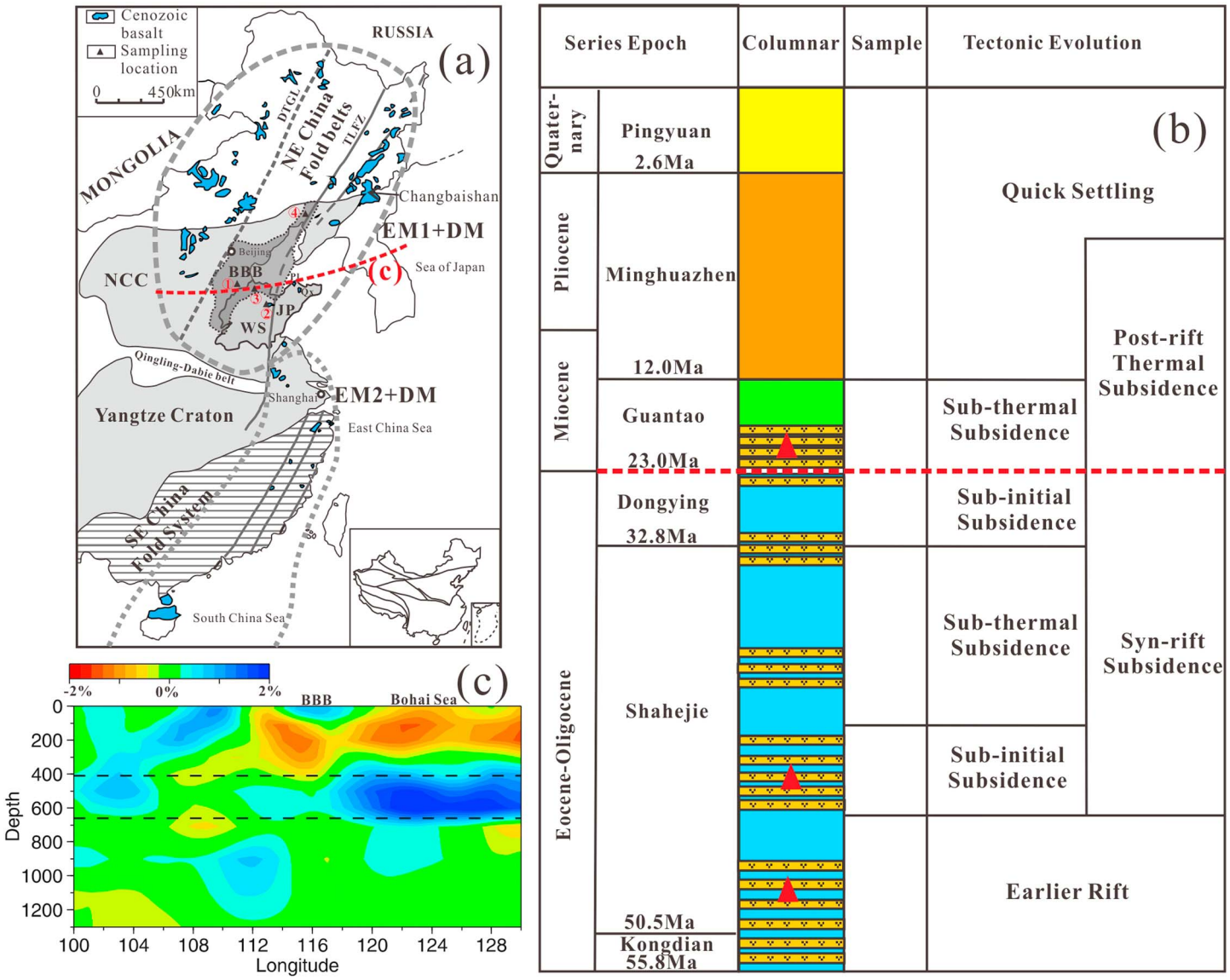

Figure 1. (a) Simplified geological map of eastern China with distributions of Cenozoic basalts and their mantle components (modified after *Li et al.* [2016a]). Sample locations are marked in black triangles: (1), Borehole samples of Jiyang Sag; (2), Changwei depression; (3), Dashan of Wudi; and (4), Borehole samples of Liaohe Sag. NCC: North China Craton; BBB: Bohai Bay Basin; WS: Western Shandong; JP: Jiaodong Peninsula; DTGL: Daxinganling-Taihang Gravity Lineament; TLFZ: Tan-Lu Fault Zone; Pl: Penglai; Qx: Qixia. The distribution of mantle components in the source of Cenozoic basalts in eastern China is after *Qin* [2008] and *Chen et al.* [2009]. (b) Cenozoic strata column of the Bohai Bay Basin with summary of the tectonic evolution (modified after *Hu et al.* [2001]), showing the approximate sample locations. (c) Vertical cross section of *P* wave velocity perturbations along the profile shown in Figure 1a map (modified after *Huang and Zhao* [2006]).

advocating that the low *P* wave velocity of shallower upper mantle is resulted from wet upwelling from the MTZ, triggered by dehydration of the stagnant Pacific slab. They also propose the EMI (isotopically enriched component) signatures in basaltic lavas erupted in northeast China are derived from the MTZ through the advocated wet upwelling [e.g., *Zhao et al.*, 2009; *Kuritani et al.*, 2011; *Liu et al.*, 2015]. Major arguments in this regard include (1) basalts of the central Changbaishan region that are more enriched in fluid mobile elements, e.g., Ba, Sr, and Pb, than basalts from other nearby regions [*Kuritani et al.*, 2011] and (2) the presence of a clear *P* wave low-velocity anomaly beneath the active Changbaishan volcano in northeast China (see location in Figure 1a), which is evident in the upper mantle down to about 410 km [*Zhao et al.*, 2009; *Huang and Zhao*, 2006]. However, recent high-resolution *P* wave tomography shows that the low-velocity anomaly beneath Changbaishan penetrates the MTZ into the lower mantle [*Tang et al.*, 2014]. Water content studies reveal that the subcontinental lithospheric mantle beneath the eastern NCC was water rich (>1000 μg/g) at

~120 Ma [*Xia et al*., 2013]. However, the water contents of the NCC lithospheric mantle became markedly lower in the Cenozoic (25 ± 18 μg/g) [*Xia et al*., 2010]. Thus, a wet upwelling event during the late Cenozoic beneath the NCC is unlikely. In addition, the isotopically enriched components of eastern China basalts delineates a strong provinciality: the isotopically enriched component in northeastern China basalts has an EMI signature, while southeastern China basalts show evidence for the involvement of an EMII (Enriched mantle type II) mantle component (Figure 1a). Therefore, it is untenable to simply attribute the isotopically enriched components of eastern China basalts to wet upwelling from the MTZ, because both the northern and southern parts of eastern China have similar mantle tomographic structures [*Li and van der Hilst*, 2010; *Zhao*, 2012; *Lei*, 2012]. In this paper we systematically examine the chemistry of Cenozoic basalts erupted in the eastern NCC as a function of time, to try to characterize the chemical evolution of the mantle reservoirs beneath the NCC and to connect that evolution and resultant mantle heterogeneity to the observed geophysical heterogeneities beneath this region.

2. Geological Background

The NCC is located in the central part of eastern China (Figure 1) and is one of the world's oldest cratons (~3.8 Ga) [*Liu et al*., 1992]. In the eastern NCC, a thick lithosphere (~200 km) with a low thermal gradient (~40 mW/m^2) is evidenced by the occurrence of refractory peridotite xenoliths enclosed in ~470 Ma diamondiferous kimberlites [e.g., *Griffin et al*., 1992, 1998; *Menzies et al*., 1993; *Xu*, 2001]. In contrast, a thin lithosphere (80–120 km) with a high thermal gradient (~60 mW/m^2) is constrained by the fertile, oceanic-type peridotites entrained in late Cenozoic basalts [e.g., *Fan and Hooper*, 1991; *Menzies and Xu*, 1998; *Griffin et al*., 1998; *Xu*, 2001], which are consistent with the present seismically determined lithospheric thickness [*Chen*, 2010] and heat flow values derived from vitrinite reflectance and apatite fission track data [*Hu et al*., 2001]. These combined data indicate considerable lithospheric thinning beneath the eastern NCC since ~470 Ma ago.

Although the timing of lithospheric thinning of the eastern NCC is controversial [e.g., *Wu et al*., 2008; *Xu et al*., 2009], the early Cenozoic is considered an important period of transition between lithospheric thinning and thickening in the eastern NCC [*Xu et al*., 2004; *Li et al*., 2014]. Based on the relationship between faulting and sedimentary sequences, the Bohai Bay Basin (BBB) in the eastern NCC experienced episodic rifting from the middle Paleocene to ~23 Ma in association with regional extension. From ~23 Ma to the present, the BBB has undergone a postrift phase of thermal subsidence with mainly strike-slip faulting activity [*Allen et al*., 1997; *Qi and Yang*, 2010]. Thermal histories derived from vitrinite reflectance and apatite fission track data suggest that the BBB experienced a period of much higher paleoheat flow (70–90 mW/m^2) at ~23 Ma and subsequent thermal decay to the present-day value of ~63 mW/m^2 [*Hu et al*., 2001]. As there is an inverse correlation between heat flow values and the seismic lithospheric thickness of the NCC [*He*, 2015], the paleoheat flow data indicates that extension in the eastern NCC resulted in lithospheric thinning before ~23 Ma, and subsequent thermal decay likely led to vertical lithospheric accretion as suggested by *Xu* [2001] and *Xu et al*. [2009].

Two episodes of Cenozoic basaltic magmatism are recorded in the BBB region in the eastern NCC (Figure 1a) [*Li et al*., 2014], one during the rifting in the BBB and a second episode that followed rifting and occurred both in and surrounding the BBB. Basaltic lavas erupted in the BBB during and after rifting were buried by sediments (Figure 1c) [*Li et al*., 2014]. From bottom to top, the Cenozoic sedimentary strata include the Kongdian (Eocene, 55.8–50.5 Ma), Shahejie (Eocene-Oligocene, 50.5–32.8 Ma), Dongying (Oligocene, 32.8–23.0 Ma), Guantao (Miocene, 23.0–12.0 Ma), Minghuazhen (Miocene-Pliocene, 12.0–2.6 Ma), and Pingyuan (Quaternary, 2.6–0 Ma) formations [*Hu et al*., 2001] (Figure 1c). The basaltic samples discussed in this study were collected from industrial boreholes in the Jiyang Sag of the southeastern BBB and in the Liaohe Sag of the northeastern BBB and belong to the Shahejie and Guantao formations.

Cenozoic basalt outcrops in Shandong, southeast of the BBB, erupted predominantly after the Oligocene and after rifting of the BBB. Alkali olivine basalts and basanites of 21–10.3 Ma erupted from numerous larger volcanoes distributed within small depressions along the Tan-Lu Fault Zone (Figure 1a), while 8.7–0.3 Ma basanites and nephelinites erupted as small isolated cones away from the Tan-Lu Fault Zone [*Zeng et al*., 2010, 2011; *Xu et al*., 2012b; *Sakuyama et al*., 2013]. In this study, the Cenozoic basalts erupted in Shandong are included among the eruptions that occurred along the periphery of the BBB.

3. Sample Selection and Petrography

BBB samples were selected for both $^{40}Ar/^{39}Ar$ dating and for elemental and isotopic geochemical characterization. Samples Y2511 and Y180 were recovered from two well-studied boreholes (Y25 and Y18) at depths of 2382 m and 2523 m, respectively, and are similar to the previously dated samples Y2510 (45.5 ± 0.8 Ma, 2360 m) and Y181 (46.9 ± 0.8 Ma, 2546 m) [*Li et al*., 2014]. The other samples from the Jiyang Sag area are from boreholes CG12, CH39, G40, Y161, Y1812, GG9, and GG16. Fourteen samples (including Y2511 and Y180) from the Shahejie Formation and five samples from the Guantao Formation of the Jiyang Sag were selected for major and trace element and radiogenic Sr-Nd-Hf isotope studies. Four samples (CG12-2, Y1812-4, Y161-2, and G40-2) from the Shahejie basalts and two samples from the Guantao basalts (GG9-1 and GG16-2) of Jiyang Sag were selected for $^{40}Ar/^{39}Ar$ dating. In addition, seven basaltic samples interlayered in age-unknown Cenozoic formations of the Jiyang Sag and six basaltic samples interlayered in the Shahejie Formation of Liaohe Sag were selected for Hf-Nd isotope analyses.

All our basaltic samples are porphyritic with a highly variable phenocryst assemblage. Olivine is observed in only the Guantao samples, while clinopyroxene and plagioclase phenocrysts are present in all samples. Most olivine and clinopyroxene phenocrysts have been partially altered to iddingsite and serpentine. Microlitic clinopyroxene, plagioclase, and Fe-Ti oxides are the major groundmass phases. All samples are vesicular and exhibit amygduloidal textures, with carbonate amygdule fills.

4. Analytical Methods

Based on petrographic observations, the freshest samples were selected for bulk rock chemical, isotopic, and geochronologic analyses. Samples were crushed into small ~0.5 cm chips, and the freshest fragments with the least amygdales and secondary veinlets were handpicked and chosen for further cleaning. Bulk rock $^{40}Ar/^{39}Ar$ dates, major and trace element abundances, and Sr-Nd-Hf isotopic data were all obtained at the Guangzhou Institute of Geochemistry, Chinese Academy of Sciences (GIG-CAS).

4.1. $^{40}Ar/^{39}Ar$ Dating

Rock chips of samples chosen for $^{40}Ar/^{39}Ar$ dating were powdered to 60–80 mesh, leached with 10% HNO_3, washed with deionized water in an ultrasonic bath, and dried. $^{40}Ar/^{39}Ar$ dating was carried out using a GVI5400 mass spectrometer following the analytical procedures described by *Qiu and Jiang* [2007]. Argon gas was extracted from the sample by stepwise heating using a MIR10 CO_2 continuing laser. The released gases were purified by two Zr/Al getter pumps operated for 5 to 8 min at room temperature and ~450°C, respectively. The background of the sample hold is lower than 2 mV preexperiment and 4–6 mV during the experiments (after a 5 min vacuum), while sample signal is mostly maintained within the range of 40–200 mV. The ArArCALC program [v. 2.2; *Koppers*, 2002] was used for data reduction and age calculation. The *J* values for the samples were determined by ZBH-2506 biotite (132 Ma) flux monitors.

4.2. Bulk Rock Major and Trace Element Chemistry

Rock chips were leached with 1% HCl and washed ultrasonically in deionized water before being dried and powdered to 200 mesh in a corundum mill. Fusion beads were prepared using a Rigaku desktop fusion machine. Bulk rock major element abundances were measured using a Rigaku RIX 2000 X-ray fluorescence spectrometer (XRF). After acid digestion of samples in high-pressure Teflon vessels, trace element abundances were measured using a Perkin-Elmer Sciex ELAN 6000 quadrupole inductively coupled plasma mass spectrometer (ICP-MS). A detailed description of the ICP-MS analytical methods is provided in *Li et al*. [2005].

4.3. Radiogenic Isotopes

Sample powders for Sr-Nd-Hf isotopic analysis were leached using distilled 6 N HCl for 20 min to eliminate carbonate infillings and possible alteration products. The leached samples were then centrifuged, rinsed using deionized water three times, and then evaporated and dried. About 100 mg of leached powder was dissolved in an HF-HNO_3 mixture in a Teflon beaker at 150°C for 7 days. High field strength elements, Sr, and rare earth elements were separated by ion chromatography using AG50-X8 cation exchange resin. Separation of Nd and Hf was carried out on a HDEHP-coated Kef column. The Sr, Nd, and Hf isotopic ratios were measured on a Neptune multicollector-ICPMS and normalized using the values of $^{86}Sr/^{88}Sr = 0.1194$, $^{146}Nd/^{144}Nd = 0.7219$, and $^{179}Hf/^{177}Hf = 0.7325$, respectively. Reference standard solutions analyzed along

with samples gave $^{87}Sr/^{86}Sr = 0.710256 \pm 5$ ($n = 6$) for NIST SRM 987, $^{143}Nd/^{144}Nd = 0.512088 \pm 4$ ($n = 5$) for Shin Etsu JNdi-1, and $^{176}Hf/^{177}Hf = 0.282190 \pm 4$ ($n = 7$) for JMC 14374 (errors are given as standard deviation). Rock standard BHVO-2 was used to monitor the ion exchange chromatographic purification processes. Analysis of BHVO-2 gave $^{87}Sr/^{86}Sr = 0.703491 \pm 5$, $^{143}Nd/^{144}Nd = 0.512979 \pm 6$, and $^{176}Hf/^{177}Hf = 0.283099 \pm 4$ (errors are given as standard error), respectively, in agreement with recommended values of $^{87}Sr/^{86}Sr = 0.703481 \pm 20$, $^{143}Nd/^{144}Nd = 0.512983 \pm 10$, and $^{176}Hf/^{177}Hf = 0.283096 \pm 20$ [*Weis et al.*, 2005].

5. Results

5.1. $^{40}Ar/^{39}Ar$ Geochronology

The $^{40}Ar/^{39}Ar$ dating results for the four Shahejie samples (CG12-2, Y1812-4, Y161-2, and G40-2) and the two Guantao samples (GG9-1 and GG16-2) are presented in Table S1 of the supporting information and are plotted in Figures 2 and 3. Initial argon compositions have $^{40}Ar/^{36}Ar$ ratios identical to atmospheric $^{40}Ar/^{36}Ar$ (295.5 ± 0.5) within error, indicating that excess argon is insignificant in the samples (Figures 2 and 3). Plateau ages of the six samples are all identical to their isochron ages (and reverse isochron ages, not shown) within error and are interpreted as the eruption ages of the basalts (Figures 2 and 3). Dating results of the Shahejie samples (CG12-2: 43.61 ± 0.78 Ma; Y1812-4: 49.16 ± 7.65 Ma; Y161-4: 44.90 ± 1.73 Ma; and G40-2: 41.95 ± 4.43 Ma) are similar to those of previously dated borehole samples from Shahejie Formation of the Jiyang Sag (Y2510, 45.5 ± 0.8 Ma; Y181, 46.9 ± 0.8 Ma) [*Li et al.*, 2014] and are in agreement with the stratigraphic age of the formations based on apatite fission track ages and K-Ar ages (50.5 − 32.8 Ma) [*Hu et al.*, 2001]. The Eocene eruption ages of the Shahejie basalts in the Jiyang Sag are significant as they are much older than the volcanic rocks on the periphery of the Bohai Bay Basin; e.g., basalts in Shandong were erupted in late Cenozoic (21.0 − 0.3 Ma) [*He et al.*, 2011]. Dating results of the Guantao samples (GG9-1: 22.95 ± 1.16 Ma and GG16-2: 23.07 ± 1.41 Ma) are close to the formation boundary age of ~23 Ma between the Dongying and Guantao formations [*Hu et al.*, 2001] (Figure 1c), and are similar to the earliest alkali olivine basalt in Shandong that erupted at ~ 21 Ma [*He et al.*, 2011; *Xu et al.*, 2012b].

5.2. Bulk Rock Chemical Composition and the Effects of Secondary Alteration

Bulk rock major and trace element analyses of the Jiyang Sag basalts are presented in Table 1. The bulk rock chemical compositions of samples of this study are plotted with those of Shandong basalts, to highlight their geochemical differences. All major element oxides are normalized on a volatile-free basis in our geochemical plots.

The Eocene samples have overall higher loss on ignition values (LOI) (2.3–7.8 wt %) than the Miocene samples (1.1–2.0 wt %; except GG9-2 = 3.2 wt %). The high LOI of some Eocene samples, as well as abundant secondary minerals, likely records varying degrees of alteration. The effects of alteration on the major element compositions are examined via their Chemical Index of Weathering ($CIW = Al_2O_3/(Al_2O_3 + CaO + Na_2O)$, molecular ratio) [*Harnois*, 1988]. Positive correlations between SiO_2, K_2O, and CIW and negative correlations between CaO, Na_2O, and CIW of samples from individual boreholes (samples Y1812-2, Y1812-3, and Y1812-4 from borehole Y1812; samples Y161-2 and Y161-4 from borehole Y161; and CG12-1 and CG12-2 from borehole CG12) suggest that secondary alteration resulted in enrichment of SiO_2 and K_2O but depletion of Na_2O and CaO in these samples (Figure S1 of the supporting information). However, their MgO and $Fe_2O_3^T$ were essentially immobile since there is no obvious correlation between them and their CIW values. The relatively low LOI and CIW values for other samples suggest that their major element compositions were little affected by secondary alteration processes (Figure S1 of the supporting information). The three Eocene samples Y180, Y1812-1, and Y2511 (with 4.0%, 4.2%, and 4.8% LOI, respectively), which have suffered comparatively little alteration, are plotted in a different color to distinguish them from the other Eocene samples in our geochemical plots (Figures 4, 5, and 7–10).

Following the nomenclature of *Le Bas et al.* [1986], the Eocene samples are alkali basalts and trachybasalts, and the Miocene samples are all tholeiitic basalts (Figure 4a). The three fresh Eocene samples plot in the field of alkali basalt on the alkali content versus SiO_2 plot (Figure 4a). As the Miocene samples have low LOI (1.1–2.0 wt %; except GG9-2 = 3.2 wt %), their tholeiitic classification appears sound. On a 2Nb-Zr/4-Y diagram, the Eocene samples plot within the "within-plate alkaline basalts" field, while the Miocene samples plot in the "within-plate alkaline basalts and tholeiites" field (Figure 4b).

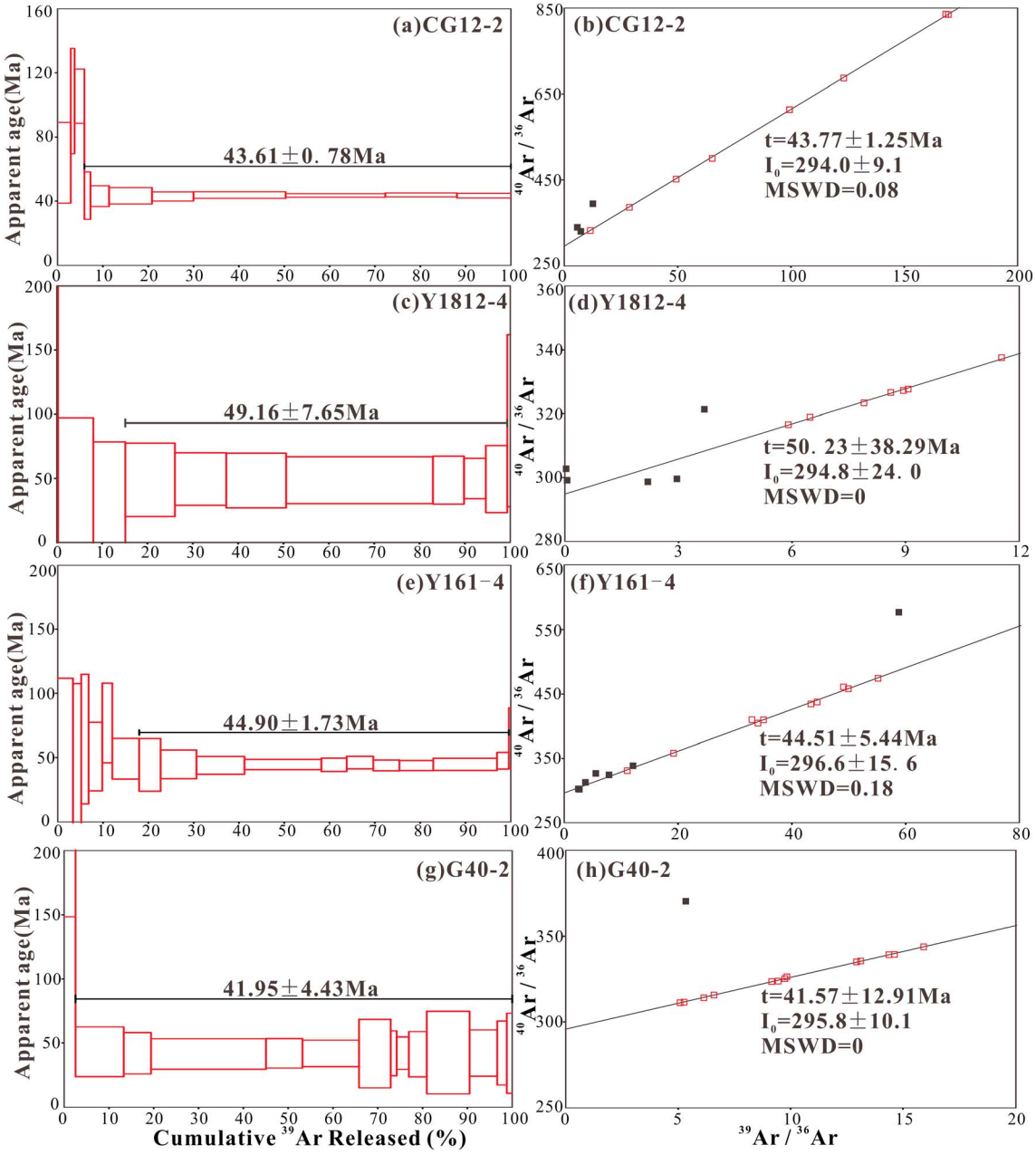

Figure 2. (a, c, e, g) Whole-rock ^{40}Ar-^{39}Ar plateau age spectra and (b, d, f, h) plots of $^{40}Ar/^{36}Ar$ versus $^{39}Ar/^{36}Ar$ for the Shahejie basalts from Jiyang Sag.

As the MgO and $Fe_2O_3^T$ contents of the Jiyang Sag basalts were little affected by alteration, their $Mg^{\#}$ values (defined as $Mg^{\#} = 100 \times Mg/(Mg + 0.85 \times Fe^{total})$, where Mg and Fe are molar concentrations) basically reflect that of their protoliths. The Miocene samples from Jiyang Sag have higher SiO_2 but otherwise largely similar bulk rock major oxide concentrations at a given $Mg^{\#}$, compared to the Miocene alkali basalts from Shandong (Figure 5). On the $Fe_2O_3^T$ and CaO/ SiO_2 versus $Mg^{\#}$ plots, the Miocene Jiyang Sag samples fall within the fields of the Miocene Shandong alkali basalts (Figures 5d and 5f). The Eocene Jiyang Sag lavas have higher SiO_2 and Al_2O_3 but lower MgO and $Fe_2O_3^T$ concentrations at a given $Mg^{\#}$ value than the basalts from Shandong (Figures 5a–5d). The three relatively fresh Eocene samples, Y2511, Y180, and Y1812-1, are the most primitive among the Eocene lavas from Jiyang Sag. They are similar in CaO concentrations to the Quaternary nephelinites from Shandong but higher in CaO than the Shandong Miocene alkali basalts. Correspondingly,

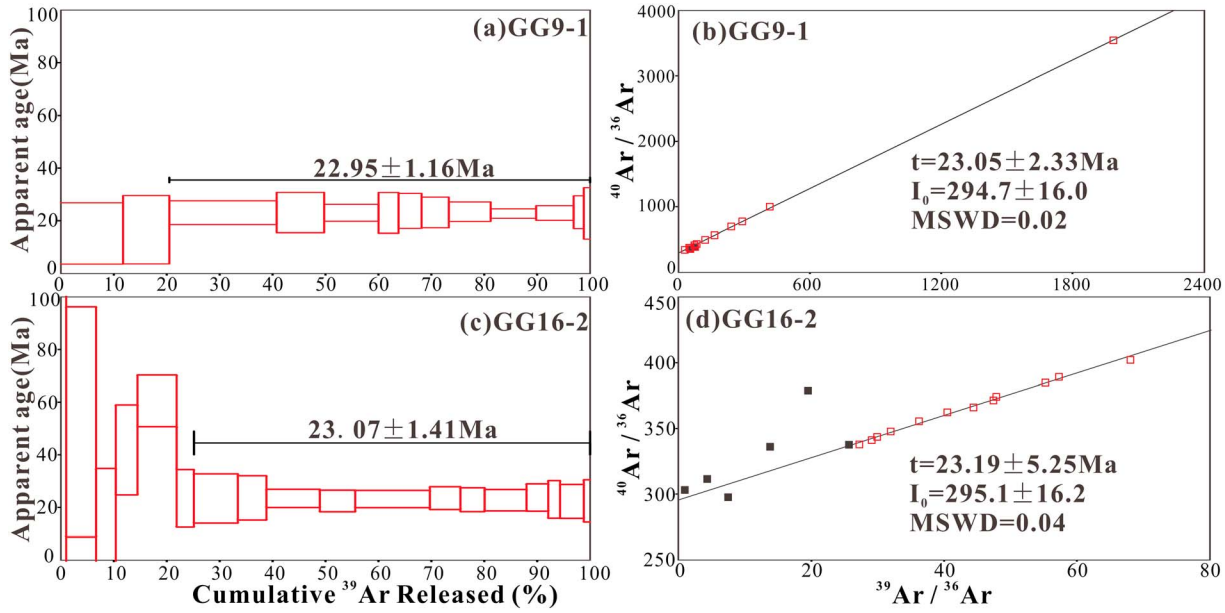

Figure 3. (a, c) Whole-rock ^{40}Ar-^{39}Ar plateau age spectra and (b, d) plots of $^{40}Ar/^{36}Ar$ versus $^{39}Ar/^{36}Ar$ for the Guantao basalts from Jiyang Sag.

these three samples have CaO/SiO_2 (Figure 5f) and CaO/Al_2O_3 ratios similar to the Miocene Shandong alkali basalts but lower values of these ratios than the Shandong nephelinites. The CaO contents and CaO/SiO_2 ratios of Eocene Jiyang Sag samples decrease sharply at $Mg^{\#} \sim 55$ (Figures 5e and 5f).

All the Jiyang Sag basalts show trace element features that are clearly different from island arc basalts (IAB) but are similar to ocean island basalt (OIB), i.e., enrichments in most incompatible elements, fractionated chondrite-normalized rare earth element (REE) patterns, and positive Nb-Ta anomalies on primitive mantle-normalized incompatible trace element diagrams (Figure 6a). All the samples also show positive Ba and Sr anomalies (Figure 6a). The Eocene basalts have higher trace element concentrations but exhibit less fractionation between middle and heavy REEs (Dy/Yb = 2.1–2.7) than do the Miocene basalts (Dy/Yb = 2.7–2.8) (Table 1 and Figure 6).

Bivariate plots of Zr against other trace elements are useful in evaluating alteration. Positive correlations between Th, U, Nb, Ta, Hf, REEs (e.g., La, Dy, Yb and Lu; Figure 7), and Zr are evident among the Eocene basalts from Jiyang Sag, apart from the highly altered samples Y1812-2, Y1812-3, and Y1812-4 (see discussion above and Figure S1 of the supporting information) which only slightly deviate from these correlations, indicating that these elements were little affected by alteration. Furthermore, the Shandong basalts have nearly constant Yb and Lu coupled with a wide range of Zr and the Miocene samples from Jiyang Sag show similar correlations between Yb, Lu, and Zr as the Shandong basalts (Figures 7c and 7d).

5.3. Sr-Nd-Hf Isotopes

Bulk rock Sr-Nd-Hf isotope analyses are presented in Table 2 and shown graphically in Figure 8. The lack of any correlation between Sr-Nd-Hf isotopic ratios with their CIW values for Jiyang Sag suggests that these samples essentially preserve their protolith Sr-Nd-Hf isotopic composition (see $\varepsilon_{Hf}(t)$ versus CIW diagram in Figure S1 of the supporting information). The Jiyang Sag basalts plot between EMI and a depleted mid-ocean ridge basalt (MORB) source on the $^{87}Sr/^{86}Sr(t)$-$\varepsilon_{Nd}(t)$ isotope plot, as do the Shandong basalts (Figure 8a). The Miocene basalts in the Jiyang Sag have overall lower $\varepsilon_{Nd}(t)$ and $\varepsilon_{Hf}(t)$ values than the Eocene basalts and fall along the trend of Shandong basalts in terms of Hf-Nd isotopes (Figure 8b). The Eocene basalts in the Jiyang Sag have higher $\varepsilon_{Hf}(t)$ value at a given $\varepsilon_{Nd}(t)$ than the Miocene Shandong and Jiyang Sag basalts, comprising a unique trend (Figure 8b). The Hf-Nd isotopes of undated samples in the Jiyang Sag also fall on the trend of the Eocene basalts. The five samples from the Liaohe Sag exhibit a broader range of $\varepsilon_{Hf}(t)$ and $\varepsilon_{Nd}(t)$ values than Jiyang Sag basalts, with two samples following the trend of the Eocene basalts (Figure 8b).

Table 1. Major (wt %) and Trace Element (ppm) Concentrations of the Jiyang Sag Basalts[a]

	Shahejie							
Sample	CG12-1	CG12-2	G40-2	G40-3	Y161-2	Y161-4	Y1812-1	Y1812-2
SiO_2	47.88	49.32	49.89	49.92	42.99	44.86	46.89	45.86
TiO_2	1.91	1.96	1.88	1.76	2.07	2.19	1.72	1.91
Al_2O_3	14.71	14.79	15.08	13.91	15.00	16.08	14.62	16.28
$Fe_2O_3^T$	11.69	10.41	10.23	10.23	10.54	8.16	9.80	9.75
MnO	0.11	0.11	0.14	0.14	0.16	0.14	0.13	0.13
MgO	4.98	5.28	5.21	5.78	5.96	5.03	6.94	5.34
CaO	7.12	10.35	8.16	7.84	9.28	9.05	9.92	7.56
Na_2O	2.87	3.29	4.21	4.56	3.37	2.85	3.16	2.35
K_2O	2.19	1.40	1.49	1.51	2.59	3.09	1.49	3.19
P_2O_5	0.38	0.40	0.40	0.38	0.74	0.82	0.31	0.65
LOI	6.16	2.27	3.00	3.65	7.34	7.78	4.75	6.88
Total	99.98	99.60	99.69	99.67	100.04	100.04	99.75	99.92
$Mg^{\#}$	49.8	54.2	54.2	56.9	56.8	59.0	62.3	56.1
Sc	22.1	25.6	21.9	21.3	22.0	23.4	24.4	20.8
Cr	278	287	138	153	154	162	268	176
Co	21	44	40	36	51	58	49	41
Ni	106	154	51	65	120	132	158	98
Rb	218.5	48.7	30.1	24.5	40.4	52.5	15.9	61.6
Sr	928	710	576	595	807	1001	655	1096
Y	18.8	21.5	18.8	18.4	22.9	26.4	18.3	21.5
Zr	143	161	153	147	202	234	143	249
Nb	25.1	28.2	31.4	30.0	69.5	80.6	27.7	71.7
Cs	8.8	3.1	3.1	2.1	0.6	0.8	0.6	0.6
Ba	486	391	639	597	925	1131	374	1235
La	19.0	21.1	25.0	23.6	43.1	50.2	18.2	46.5
Ce	40.5	44.5	50.4	47.2	81.0	96.1	37.7	84.0
Pr	5.36	5.85	6.39	6.03	9.84	11.40	4.81	9.51
Nd	23.2	25.6	26.1	25.0	37.8	44.0	20.3	35.5
Sm	5.27	5.70	5.61	5.36	6.74	7.95	4.49	6.30
Eu	1.71	1.90	1.77	1.72	2.08	2.45	1.56	1.94
Gd	5.01	5.59	5.07	4.98	5.66	6.82	4.54	5.16
Tb	0.77	0.85	0.78	0.75	0.87	1.03	0.71	0.79
Dy	4.24	4.60	4.20	4.10	4.86	5.69	3.98	4.49
Ho	0.83	0.90	0.79	0.77	0.97	1.15	0.78	0.91
Er	2.05	2.17	1.92	1.92	2.46	2.90	2.01	2.32
Tm	0.29	0.30	0.27	0.26	0.35	0.41	0.28	0.34
Yb	1.78	1.78	1.58	1.53	2.11	2.46	1.62	2.13
Lu	0.25	0.26	0.22	0.21	0.31	0.37	0.24	0.32
Hf	3.31	3.88	3.69	3.54	4.56	5.47	3.46	5.38
Ta	1.63	1.78	2.11	2.02	4.29	5.11	1.83	4.85
Pb	1.82	3.31	3.29	5.47	2.69	3.84	2.57	4.19
Th	1.92	2.21	3.24	3.13	5.06	6.10	2.06	7.62
U	0.56	0.58	0.84	0.78	1.23	1.52	0.60	1.84
CaO/Al_2O_3	0.48	0.70	0.54	0.56	0.62	0.56	0.68	0.46
CaO/SiO_2	0.15	0.21	0.16	0.16	0.22	0.20	0.21	0.16
Th/Nb	0.08	0.08	0.10	0.10	0.07	0.08	0.07	0.11
La/Yb	10.7	11.8	15.8	15.4	20.4	20.4	11.3	21.9
Dy/Yb	2.4	2.6	2.7	2.7	2.3	2.3	2.5	2.1
Y/Yb	10.5	12.1	11.9	12.0	10.8	10.7	11.3	10.1

[a] $Fe_2O_3^T$ is total iron as Fe_2O_3. $Mg^{\#}=100*Mg/(Mg+0.85*Fe^{total})$, where Mg and Fe are molar concentrations. GG16-2 is from *Li et al.* [2016a].

6. Discussion

6.1. Contamination and Fractional Crystallization

As discussed above, secondary alteration processes affected the bulk major element compositions of the Eocene samples from Jiyang Sag. The main effects are elevated LOI, K_2O, and SiO_2 and lowered CaO and Na_2O. However, their $Mg^{\#}$ value and Th, U, Nb, Ta, Hf, REE, and Zr contents appear not to be significantly affected by alteration. The Miocene samples from Jiyang Sag, by contrast, preserve their protolith chemical

Table 1. Major (wt %) and Trace Element (ppm) Concentrations of the Jiyang Sag Basalts[a]

Shahejie				Guantao				
Y1812-3	Y1812-4	Y180	Y2511	GG16-1	GG16-2	GG16-3	GG9-1	GG9-2
45.64	45.73	46.20	46.60	49.60	50.19	49.90	48.26	47.71
1.99	1.86	1.97	1.73	1.73	1.75	1.72	1.72	1.69
16.79	16.05	14.38	14.94	13.40	13.33	13.29	13.14	13.43
9.99	10.31	11.35	10.41	11.78	11.15	11.81	11.54	11.50
0.12	0.14	0.12	0.15	0.15	0.13	0.16	0.15	0.14
4.83	5.42	7.69	7.90	9.05	8.77	8.77	10.27	9.81
6.49	8.75	9.22	9.28	9.29	9.17	9.13	8.54	8.22
2.33	2.51	2.71	2.78	2.70	2.62	2.71	2.54	2.45
3.38	2.63	1.55	1.41	0.52	0.58	0.47	1.07	1.12
0.69	0.63	0.35	0.47	0.25	0.27	0.26	0.32	0.33
7.83	5.76	4.21	4.01	1.07	1.64	1.36	2.04	3.21
100.07	99.80	99.74	99.69	99.56	99.60	99.57	99.59	99.61
53.0	55.1	61.2	63.9	64.2	64.7	63.4	67.5	66.5
21.5	22.2	25.0	24.6	23.7	23.5	22.0	23.6	23.9
173	193	232	296	316	340	290	366	355
42	41	52	48	57	54	55	58	58
106	97	194	127	202	201	187	250	252
72.5	47.9	21.3	10.0	2.8	4.3	2.7	15.2	15.0
1187	1327	788	706	406	410	392	402	384
21.8	22.2	18.4	20.8	17.1	17.4	17.2	16.9	17.2
270	241	145	180	115	120	112	129	129
76.8	68.9	28.7	47.9	18.2	18.9	17.0	22.7	23.2
0.8	0.7	0.3	0.3	0.0	0.1	0.0	0.1	0.1
1025	2117	386	442	210	217	200	248	239
49.4	45.1	20.2	31.4	14.7	15.8	14.5	18.6	18.9
88.5	82.9	40.5	59.6	30.8	33.0	30.2	38.8	39.1
9.95	9.36	5.21	6.90	4.01	4.30	3.93	4.98	5.00
36.4	35.5	21.6	27.0	17.3	18.5	17.1	21.1	21.2
6.51	6.33	4.71	5.26	4.21	4.51	4.23	4.75	4.82
1.98	1.82	1.62	1.72	1.50	1.61	1.45	1.61	1.62
5.21	5.33	4.72	4.84	4.53	4.64	4.41	4.58	4.50
0.81	0.82	0.72	0.75	0.67	0.70	0.69	0.70	0.68
4.64	4.55	4.01	4.32	3.77	3.90	3.86	3.73	3.76
0.93	0.91	0.80	0.84	0.74	0.75	0.74	0.71	0.72
2.37	2.37	1.96	2.21	1.77	1.76	1.79	1.71	1.70
0.36	0.35	0.27	0.32	0.24	0.24	0.24	0.24	0.23
2.21	2.10	1.66	1.86	1.37	1.43	1.44	1.34	1.39
0.33	0.32	0.24	0.29	0.20	0.20	0.21	0.19	0.20
5.75	5.22	3.58	3.92	3.02	3.13	3.03	3.21	3.23
5.25	4.58	1.94	2.96	1.22	1.30	1.16	1.53	1.57
4.16	3.81	2.95	3.03	2.77	2.01	1.88	1.94	2.38
8.46	7.29	2.23	3.46	1.83	1.94	1.82	2.01	2.03
2.05	1.74	0.65	0.93	0.39	0.40	0.40	0.52	0.42
0.39	0.55	0.64	0.62	0.69	0.69	0.69	0.65	0.61
0.14	0.19	0.20	0.20	0.19	0.18	0.18	0.18	0.17
0.11	0.11	0.08	0.07	0.10	0.10	0.11	0.09	0.09
22.4	21.5	12.1	16.9	10.8	11.1	10.1	13.8	13.6
2.1	2.2	2.4	2.3	2.8	2.7	2.7	2.8	2.7
9.9	10.6	11.1	11.2	12.5	12.2	12.0	12.6	12.3

compositions. As compared to their wide range of $\varepsilon_{Nd}(t)$ values, from −1.3 to +6.0, the Jiyang Sag and Shandong basalts have nearly constant Th/Nb ratios (0.07–0.14 and 0.06–0.10, respectively) that are much lower than the value for bulk continental crust (Th/Nb = 0.70) [*Rudnick and Gao*, 2003] but similar to values for OIBs (Th/Nb = 0.08) [*Sun and McDonough*, 1989]. Melt inclusions hosted in the olivines of tholeiite sample GG16-2 have lower TiO_2 (1.0 ~ 2.7%) and K_2O/TiO_2 (0.1 ~ 0.6) than the basanites and nephelinites (TiO_2 of 2.8 ~ 3.9%; K_2O/TiO_2 of 0.4 ~ 0.8) [*Li et al.*, 2016a]. Therefore, the tholeiites cannot be generated via contamination of lower-Si melts by the continental crust (TiO_2 of 0.7%; K_2O/TiO_2 of 2.5) [*Rudnick and Gao*,

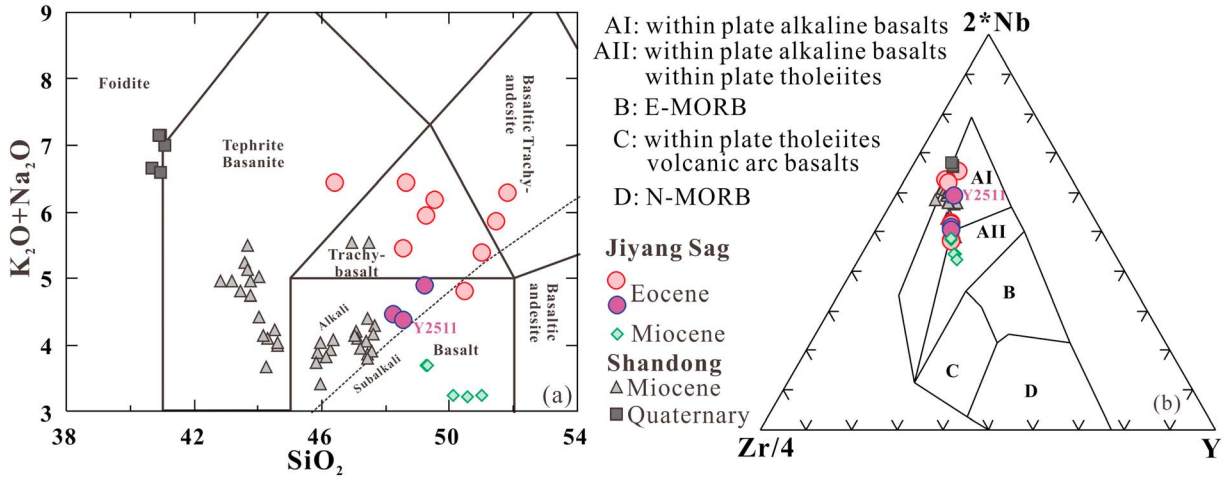

Figure 4. (a) Alkali content versus SiO_2 (following the nomenclature of *Le Bas et al*. [1986], the line separating alkali basalts and tholeiites is from *McDonald and Katsura* [1964]) and (b) Zr/4-2Nb-Y [after *Meschede*, 1986] diagrams for bulk rocks of basalts from Jiyang Sag and Shandong. Note that the three relatively fresh samples Y180, Y1812-1, and Y2511 are plotted in purple distinguishing from other Eocene samples in pink. The data of Miocene basalts in Shandong are from *Zeng et al*. [2011], and those of Quaternary Dashan nephelinite are from *Zeng et al*. [2010, 2011] and *Li et al*. [2016a]. The major element oxides are in wt %, and those of Jiyang Sag were corrected for the volatile components: $X^* = X \times 100/(100 - \mathrm{LOI})$; X and X^* are the measured and corrected values, respectively.

2003]. These features rule out crustal contamination as producing significant compositional variations within the Jiyang Sag or Shandong basalts.

The Miocene alkali basalts from Shandong, the tholeiites from Jiyang Sag, and the Quaternary nephelinites from Shandong span a relatively narrow range of $Mg^{\#}$, from 60 to 69, with different ranges of SiO_2, Al_2O_3, MgO, $Fe_2O_3^T$, and CaO (Figure 5). This suggests that these basalts have undergone only limited extents of fractional crystallization. The inverse correlations between CaO, CaO/SiO_2, and $Mg^{\#}$ (Figures 5e and 5f) of the Miocene tholeiites from Jiyang Sag indicate that these samples experienced fractional crystallization primarily of olivine, without significant clinopyroxene.

The Eocene basalts from Jiyang Sag are more evolved, with $Mg^{\#}$ of 64 to 50, than either Jiyang Sag or Shandong Miocene basalts. Inverse correlations between CaO, CaO/SiO_2, and $Mg^{\#}$ at $Mg^{\#}$ of ~64–57 (Figures 5e and 5f) suggest that even the most primitive Eocene basalts have experienced fractional crystallization of olivine. Although the sharp decrease in CaO and CaO/SiO_2 at $Mg^{\#}$ of ~55 in the evolved Eocene samples is obviously influenced by alteration processes (Figure S1 of the supporting information), the possibility of fractional crystallization of clinopyroxene during their evolution cannot be excluded. Plagioclase fractionation is insignificant, as demonstrated to some degree by the lack of negative Eu anomalies on their REE patterns (Figure 6b). The lack of correlation between Dy/Yb and $Mg^{\#}$ (Figure 9a) suggests that crystallization had little effect on the differentiation between middle and heavy REEs and between Y and Yb (Figure 9b) in the Jiyang Sag samples.

Plots of $Mg^{\#}$ against MgO and $Fe_2O_3^T$ (Figures 5c and 5d) suggest that the Eocene basalts evolved from primary magmas with low MgO and $Fe_2O_3^T$, in stark contrast to the Quaternary nephelinites from Shandong. The calculated primary magma, corrected for fractionation to $Mg^{\#} = 72$ using liquid lines of descent derived from MORB (per *Niu and O'Hara* [2008]) suggests that the parental melts of the three primitive Eocene samples (Y1812-1, Y2511, and Y180) had much lower MgO and $Fe_2O_3^T$ than those of the Quaternary nephelinites from Shandong (Figure 10).

6.2. The Role of Different Mantle Reservoirs at Different Stages of Basalt Generation

6.2.1. Controlling Factors on the Chemical Makeup of Intraplate Basalts

The basalts of this study have more enriched Hf-Nd isotopes ($\varepsilon_{Nd} = -2.7 \sim 6.6$; $\varepsilon_{Hf} = 0.75 \sim 11.2$) than mantle xenoliths discovered in Shandong basalts ($\varepsilon_{Nd} = 3.1 \sim 24.0$; $\varepsilon_{Hf} = 7.4 \sim 655$) [*Chu et al*., 2009]. This precludes the possibility of lithospheric mantle as a major source component for basalts of eastern NCC. Therefore, it is likely that our studied basalts were derived via melting of an asthenospheric mantle source. Factors controlling the primary melt compositions of intraplate basalts are still a matter under debate. Recent studies

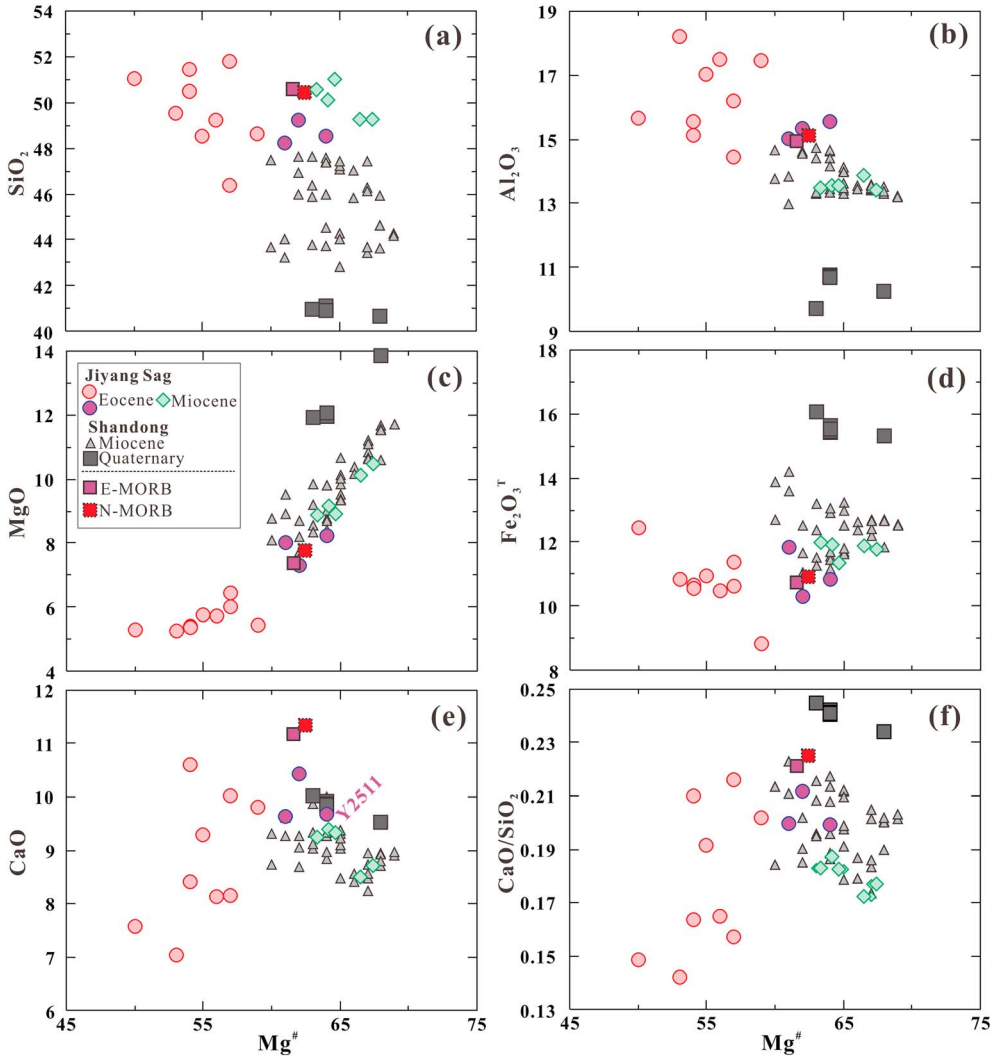

Figure 5. (a) SiO_2, (b) Al_2O_3, (c) MgO, (d) $Fe_2O_3^T$, (e) CaO, and (f) CaO/SiO_2 versus $Mg^{\#}$ diagrams for basalts from Jiyang Sag and Shandong. The major element oxides are in wt %, and those of Jiyang Sag were corrected for the volatile components. $Mg^{\#} = 100*Mg/(Mg + 0.85*Fe^{total})$, where Mg and Fe are molar concentrations. The data source of Shandong basalts is as that in Figure 4. The major elemental composition of enriched mid-ocean ridge basalts (E-MORB) and normal mid-ocean ridge basalts (N-MORB) are from *Gale et al.* [2013].

[e.g., *Kogiso et al.*, 1998, 2003; *Hirschmann et al.*, 2003; *Sobolev et al.*, 2005, 2007; *Herzberg*, 2006, 2011] have emphasized the importance of mantle pyroxenite on the initial chemical compositions of OIBs. These studies have proposed that recycled materials react with peridotite to form secondary pyroxenite, which facilitates mantle melting by locally decreasing the solidus [e.g., *Kogiso et al.*, 2003; *Hirschmann et al.*, 2003; *Sobolev et al.*, 2007]. The bulk chemistry of OIBs would therefore be dominantly controlled by the proportion of melt derived from olivine-free pyroxenites relative to that derived from peridotite [*Sobolev et al.*, 2005, 2007] or by varying the degrees of enrichment of the pyroxenite [*Herzberg*, 2011]. Based on statistical research on the global geochemical variations in OIBs, *Humphreys and Niu* [2009] and *Niu et al.* [2011] have proposed that lithospheric thickness exerts a primary control on OIB geochemistry. In this scenario, lithospheric thickness controls the final pressure of melting and correspondingly defines the bulk distribution coefficients $\left(D_{\text{element}}^{\text{bulk/melts}}\right)$ of elements in the source, which ultimately governs the geochemistry of OIBs; hence, olivine-free pyroxenite is not considered as a major source component in this model [*Niu et al.*, 2011]. However, *Sobolev et al.* [2007] noted that olivine-free pyroxenite could contribute more to basalts generated beneath a thicker lithosphere than beneath a thinner lithosphere—that is, deeper-seated melting would tap into the more melt-able pyroxenite domains preferentially. Thus, the degree to which pyroxenitic mantle domains are

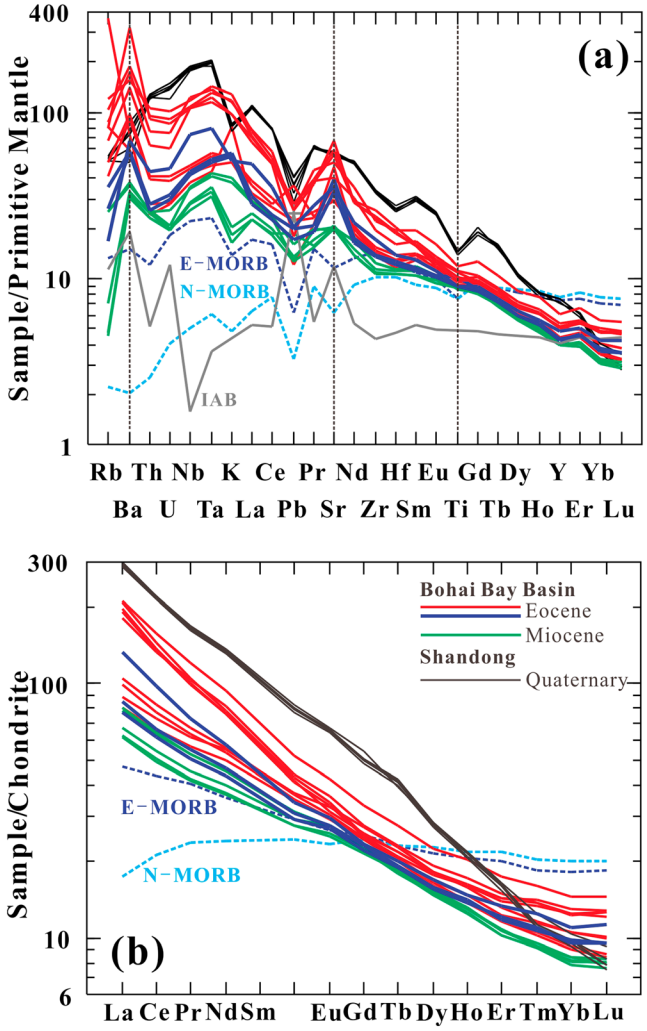

Figure 6. (a) Primitive mantle-normalized [*McDonough and Sun*, 1995] trace element patterns and (b) chondrite-normalized [*Sun and McDonough*, 1989] REE patterns of basalts from the Jiyang Sag and Shandong. Note that the three relatively fresh samples Y180, Y1812-1, and Y2511 are plotted in dark blue distinguishing from other Eocene samples in red. The data of Quaternary Dashan nephelinite are from *Zeng et al*. [2010] and *Li et al*. [2016a]. The trace elemental compositions of average MORB and Island Arc Basalt (IAB) are from *Gale et al*. [2013] and *Niu and O'Hara* [2003], respectively.

responsible for the geochemistry of intraplate basalts, and whether lithospheric thickness or source exerts the first-order constraint, remains to be clarified.

OIBs afford a straightforward means for studying lithospheric thickness effects on magma generation, as the thickness of oceanic lithospheric is relatively simply correlated with its age [e.g., *Parsons and Sclater*, 1977; *Phipps Morgan and Smith*, 1992; *Stein and Stein*, 1992]. The thickness of the oceanic lithosphere at the time of the generation of OIBs can thus be constrained, albeit in a model-dependent fashion [e.g., *Humphreys and Niu*, 2009; *Niu et al*., 2011]. For intracontinental basalts, constraining lithospheric thickness during magma generation is necessarily more difficult. In addition, the continental mantle is more spatially heterogeneous than the oceanic mantle [e.g., *Fitton*, 2007]. These features suggest that lithospheric thickness may not afford the same straightforward controls over the melting processes that generate continental intraplate basalts.

The eastern North China Craton (NCC) is an ideal region for studying the different controls on the chemical composition of intracontinental basalts for three reasons: (1) numerous petrologic, tectonic, and paleoheat flow results reveal that the eastern NCC experienced significant lithospheric thinning and thickening events during the Cenozoic [*Xu*, 2001; *Hu et al*., 2001; *Qi and Yang*, 2010; *Li et al*., 2014]; (2) these lithospheric changes coincided with long-term intracontinental basaltic magmatism both within and along the margins of the NCC, potentially recording these changes [*Wu et al*., 2005; *Zeng et al*., 2010, 2011; *Li et al*., 2014, 2016a]; and (3) the Cenozoic basalts in the eastern NCC appear to record mixing of isotopically enriched and depleted materials in varying proportions [*Zeng et al*., 2010, 2011; *Xu et al*., 2012a; *Li et al*., 2014, 2016a, 2016b].

6.2.2. Summary of the Geochemistry of the Postrifting Basalts: Mixing of Melts From Two Different Pyroxenitic Mantle Domains

The boundary age between the rifting and postrifting stages of the Bohai Bay Basin is ~23 Ma [*Hu et al*., 2001; *Qi and Yang*, 2010] (Figure 1b). The postrifting suite of basalts includes the 21–0.3 Ma alkali olivine basalts, basanites, and nephelinites in Shandong. Although Miocene tholeiites from the Jiyang Sag have $^{40}Ar/^{39}Ar$ ages of ~ 23 Ma, right on the boundary between the rifting and postrifting events of the BBB, they are treated together with the postrifting basalts in the following discussion for these reasons: (1) the rifting-stage basalts were erupted under conditions of strong asthenospheric upwelling in the mantle in association with

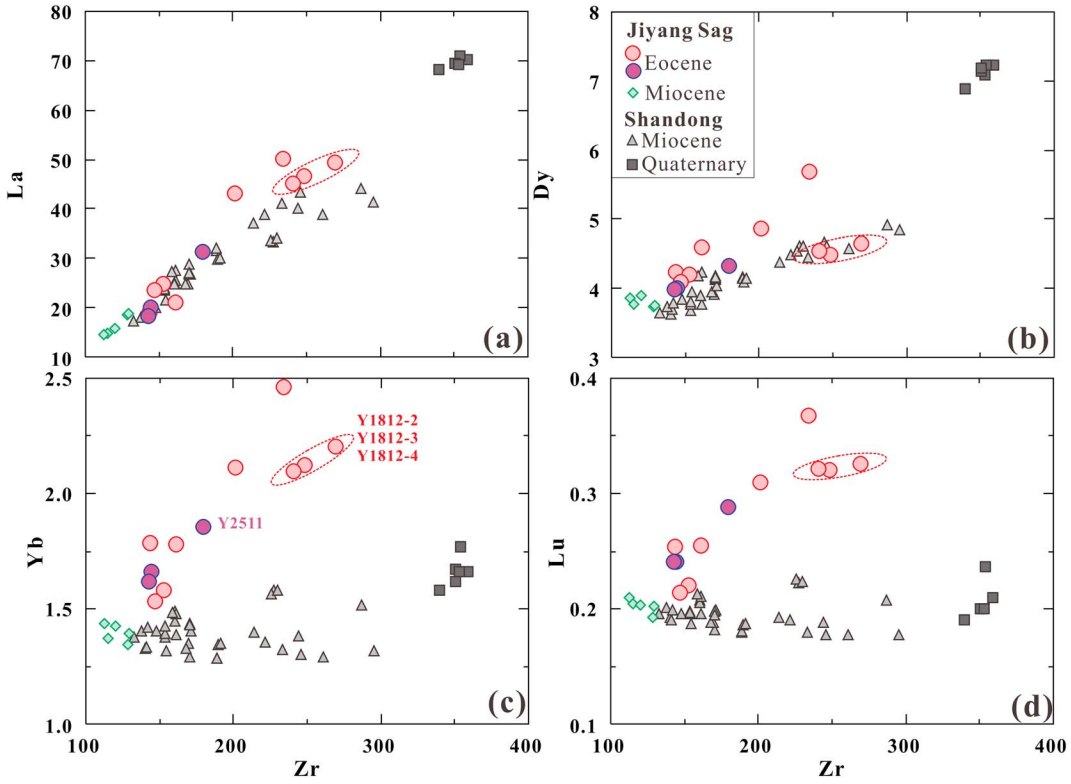

Figure 7. (a) La, (b) Dy, (c) Yb, and (d) Lu versus Zr diagrams for basalts from the Jiyang Sag and Shandong. The La, Dy, Yb, and Lu are in ppm. The data source of Shandong basalts is as that in Figure 4.

continental rifting [e.g., *Ziegler and Cloetingh*, 2004]. The Miocene tholeiites, by contrast, erupted under mantle conditions absent asthenospheric upwelling, much like the postrifting-stage basalts; (2) the tholeiites from Jiyang Sag are closer in age to the postrifting basalts of Shandong (≤21 Ma) [*He et al*., 2011] and are much younger than the rifting-stage basalts in the Jiyang Sag (49–42 Ma; Figure 2).

The postrifting basalts in the NCC have been the subject of several recent studies [e.g., *Zeng et al*., 2010, 2011; *Xu et al*., 2012b; *Sakuyama et al*., 2013; *Liu et al*., 2015; *Li et al*., 2016a, 2016b]. The bulk chemical compositions of these basalts vary systematically with their SiO_2 concentrations. The high-SiO_2 basalts have lower alkalies (Figure 4a), MgO, FeO^T, CaO and CaO/SiO_2 and higher Al_2O_3 (Figure 5) than the low-SiO_2 basalts. Compared with the low-SiO_2 basalts, the high-SiO_2 basalts also have lower trace element concentrations and less fractionated REEs (lower La/Yb and Dy/Yb; Figure 9), and lower ε_{Nd} and ε_{Hf} values (Figure 8b). Additionally, the high-SiO_2 basalts are enriched in some fluid mobile elements (e.g., Sr and Ba) [*Li et al*., 2016b]. The compositions of all these postrifting basalts are consistent with the mixing of two end-members in terms of major and trace elements and isotopes [*Zeng et al*., 2010, 2011; *Li et al*., 2016a, 2016b]. The high-SiO_2 basalts show greater contributions from an EMI-like mantle domain than do the low-SiO_2 basalts (Figure 8a) [*Zeng et al*., 2010, 2011; *Sakuyama et al*., 2013; *Li et al*., 2016a, 2016b].

The olivines from the Jiyang Sag Miocene tholeiites (GG16-2) have been shown to have lower Ca and Mn and higher Ni than those crystalized from peridotite source melts [*Li et al*., 2016a]. Their olivine melt inclusions (GG16-2) [*Li et al*., 2016a] and host bulk rocks [*Zeng et al*., 2011] have lower CaO at a given MgO than melts of peridotite, pointing to a garnet pyroxenite mantle source. These geochemical features suggest that the EMI component in these postrifting basalts was predominantly derived from a garnet pyroxenitic mantle source [*Li et al*., 2016a]. Olivines in the Quaternary nephelinites have lower Ni and higher Mn at a given Fo value than those from the Miocene tholeiites, suggesting more olivine in their source. In addition, melt inclusions within nephelinite olivines have lower SiO_2 and higher CaO and TiO_2 than do melts from a carbonate-free mantle source, which suggests that the nephelinites were likely derived from a carbonated peridotite-pyroxenite mixed mantle source [*Li et al*., 2016a], consistent with inferences others have drawn

Journal of Geophysical Research: Solid Earth

10.1002/2016JB013486

Table 2. Sr-Nd-Hf Isotopes of the Jiyang Sag and Liaohe Sag Basalts[a]

	Age	$^{87}Rb/^{86}Sr$	$^{87}Sr/^{86}Sr$	$(^{87}Sr/^{86}Sr)_t$	$^{147}Sm/^{144}Nd$	$^{143}Nd/^{144}Nd$	$(^{143}Nd/^{144}Nd)_t$	$\varepsilon_{Nd}(t)$	$^{176}Lu/^{177}Hf$	$^{176}Hf/^{177}Hf$	$(^{176}Hf/^{177}Hf)_t$	$\varepsilon_{Hf}(t)$
Jiyang Sag												
CG12-1	43.6	0.6813	0.705143	0.704721	0.1370	0.512555	0.512516	−1.3	0.01067	0.282908	0.282899	5.4
CG12-2	43.6	0.1985	0.704595	0.704472	0.1348	0.512640	0.512601	0.4	0.00913	0.282918	0.282910	5.9
G40-2	42.0	0.1511	0.704684	0.704594	0.1299	0.512626	0.512591	0.1	0.00829	0.282879	0.282872	4.5
G40-3	42.0				0.1294	0.512627	0.512592	0.1	0.00839	0.282877	0.282871	4.4
Y161-2	44.9	0.1448	0.703496	0.703403	0.1079	0.512849	0.512817	4.6	0.00944	0.282998	0.282990	8.7
Y161-4	44.9	0.1515	0.703588	0.703491	0.1093	0.512852	0.512820	4.7	0.00935	0.283000	0.282992	8.8
Y1812-1	46.9	0.0700	0.703905	0.703858	0.1340	0.512717	0.512676	1.9	0.00968	0.282952	0.282944	7.1
Y1812-2	49.2	0.1627	0.703898	0.703784	0.1072	0.512780	0.512746	3.3	0.00826	0.282987	0.282980	8.4
Y1812-3	49.2	0.1765	0.703719	0.703595	0.1081	0.512806	0.512771	3.8	0.00787	0.282986	0.282979	8.4
Y1812-4	49.2	0.1043	0.704103	0.704030	0.1079	0.512775	0.512740	3.2	0.00854	0.283001	0.282993	8.9
Y180	46.9	0.0781	0.704211	0.704159	0.1316	0.512745	0.512705	2.5	0.00935	0.282967	0.282959	7.6
Y2511	45.5	0.0411	0.703305	0.703278	0.1179	0.512881	0.512846	5.2	0.01021	0.283031	0.283022	9.9
GG16-1	23.1	0.0203	0.704352	0.704345	0.1473	0.512663	0.512641	0.6	0.00938	0.282864	0.282860	3.6
GG16-2	23.1	0.0302	0.704330	0.704320	0.1469	0.512663	0.512641	0.6	0.00900	0.282870	0.282866	3.8
GG16-3	23.1	0.0200	0.704379	0.704372	0.1495	0.512634	0.512612	0.1	0.00963	0.282861	0.282857	3.5
GG9-1	23.0	0.1093	0.703888	0.703853	0.1362	0.512610	0.512589	−0.4	0.00834	0.282860	0.282857	3.5
GG9-2	23.0	0.1129	0.703881	0.703844	0.1375	0.512621	0.512601	−0.1	0.00870	0.282863	0.282859	3.6
Jiyang Sag (age-unknown samples)												
S2901						0.512643				0.282940		
S2903						0.512640				0.282941		
S2908						0.512629				0.282944		
S2910						0.512640				0.282943		
S74201						0.512524				0.282837		
S74208						0.512609				0.282955		
S74210						0.512619				0.282964		
Liaohe Sag												
L04	40.0				0.1428	0.512783	0.512746	3.1	0.01047	0.282928	0.282920	6.1
L11	40.0				0.1333	0.512570	0.512535	−1.0	0.00802	0.282826	0.282820	2.6
L17	40.0				0.1224	0.512854	0.512822	4.6	0.00689	0.283000	0.282995	8.8
L24	40.0				0.1475	0.512486	0.512447	−2.7	0.01034	0.282776	0.282768	0.7
L29	40.0				0.1240	0.512763	0.512731	2.8	0.00876	0.283014	0.283007	9.2
L51	40.0				0.1279	0.512960	0.512927	6.6	0.00937	0.283072	0.283065	11.2

[a](1) $^{87}Rb/^{86}Sr$, $^{147}Sm/^{144}Nd$, and $^{176}Lu/^{177}Hf$ are calculated using whole-rock Rb, Sr, Sm, Nd, Lu, and Hf contents; (2) $(^{87}Sr/^{86}Sr)_{s\text{-}t} = (^{87}Sr/^{86}Sr)_s - (^{87}Rb/^{86}Sr)_s \times (e^{\lambda t} - 1)$, $\lambda(^{87}Rb) = 1.42 \times 10^{-11}\ yr^{-1}$; $(^{143}Nd/^{144}Nd)_{s\text{-}t} = (^{143}Nd/^{144}Nd)_s - (^{147}Sm/^{144}Nd)_s \times (e^{\lambda t} - 1)$, $\lambda(^{147}Sm) = 6.54 \times 10^{-11}\ yr^{-1}$; $(^{176}Hf/^{177}Hf)_{s\text{-}t} = (^{176}Hf/^{177}Hf)_s - (^{176}Lu/^{177}Hf)_s \times (e^{\lambda t} - 1)$, $\lambda(^{176}Lu) = 1.867 \times 10^{-11}\ yr^{-1}$; (3) $\varepsilon_{Nd}(t) = [(^{143}Nd/^{144}Nd)_{s\text{-}t}/(^{143}Nd/^{144}Nd)_{CHUR\text{-}t} - 1] \times 10{,}000$, $(^{143}Nd/^{144}Nd)_{CHUR} = 0.512638$, $(^{147}Sm/^{144}Nd)_{CHUR} = 0.1967$ [*Jacobsen and Wasserburg*, 1980]; $\varepsilon_{Hf}(t) = [(^{176}Hf/^{177}Hf)_{s\text{-}t}/(^{176}Hf/^{177}Hf)_{CHUR\text{-}t} - 1] \times 10{,}000$, $(^{176}Hf/^{177}Hf)_{CHUR} = 0.282772$, $(^{176}Lu/^{177}Hf)_{CHUR} = 0.0332$ [*Blichert-Toft and Albarède*, 1997].

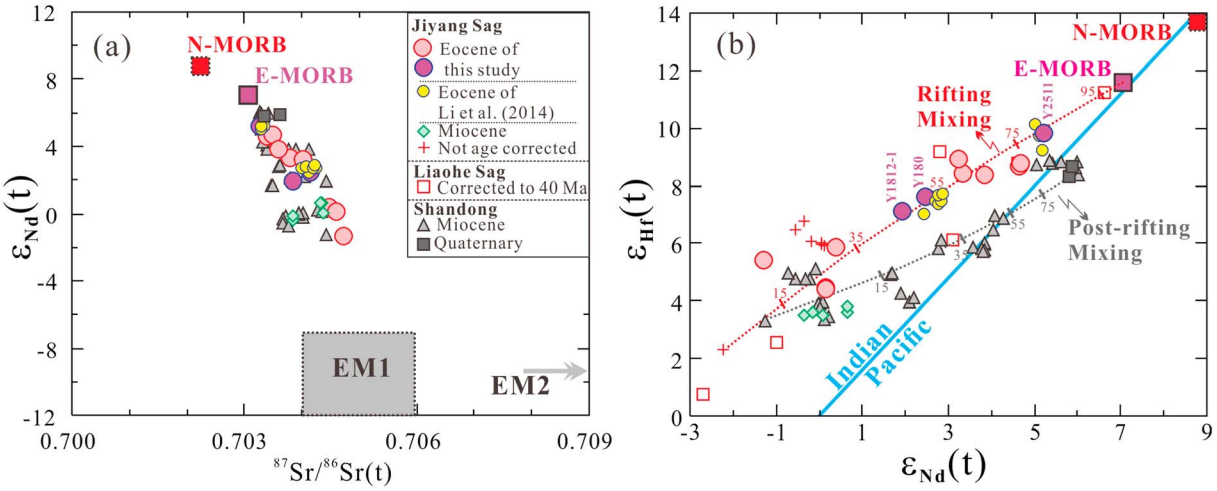

Figure 8. Diagrams of (a) $\varepsilon_{Nd}(t)$ versus $^{87}Sr/^{86}Sr(t)$ and (b) $\varepsilon_{Hf}(t)$ versus $\varepsilon_{Nd}(t)$ for basalts from the Jiyang Sag and Shandong. The data source of Shandong basalts is as that in Figure 4, with the Sr-Nd-Hf isotopic composition of Quaternary Dashan nephelinite from *Zeng et al.* [2011] as an average value. For E-MORB and N-MORB, Sr-Nd isotopic composition is according to *Su and Langmuir* [2003]; Hf isotopic composition is according to *Workman and Hart* [2005]. During mixing calculation of the rifting-stage basalts in Figure 8b, the Hf and Nd trace elemental composition of the E-MORB is according to *Gale et al.* [2013]. The ranges of EMI and EMII in Figure 8a are according to *Zindler and Hart* [1986]. The solid line in Figure 8b is the Hf-Nd isotopic boundary between the mantle reservoirs of the Indian and Pacific MORB types [*Pearce et al.*, 1999].

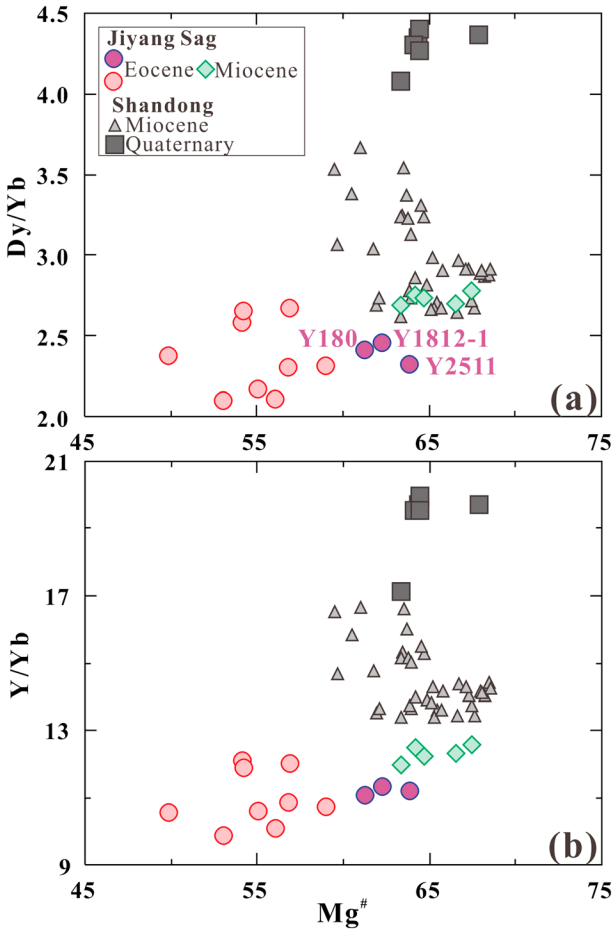

Figure 9. (a) Dy/Yb and (b) Y/Yb versus $Mg^{\#}$ diagrams for basalts from the Jiyang Sag and Shandong.

based on their bulk rock chemistries [*Zeng et al.*, 2010; *Sakuyama et al.*, 2013] and their Mg isotopes [*Yang et al.*, 2012; *Huang et al.*, 2015].

The temperature of first appearance for silicate melts from garnet pyroxenite at 3 GPa is only slightly lower (~50°C) [*Kogiso et al.*, 2003] than that of a typical mantle peridotite, while first melt appearance in carbonated eclogite sources are much lower (~150°C) [*Hirschmann*, 2000; *Dasgupta et al.*, 2006]. Thus, the generation of silicate melts from carbonated eclogite/pyroxenite can occur at greater depths than can melts of carbonate-free pyroxenite [*Dasgupta et al.*, 2006]. In addition, carbonated pyroxenite would experience higher degrees of melting than carbonate-free pyroxenite under identical mantle conditions. The Quaternary nephelines have lower Al_2O_3 along with higher MgO and $Fe_2O_3^T$ (Figure 5) and more fractionated REEs (Figure 9) at a given $Mg^{\#}$ than do the Miocene tholeiites and alkali basalts. As higher pressure melting will lead to lower SiO_2 and Al_2O_3 along with higher MgO and $Fe_2O_3^T$ at a similar value of F for melting, it is irrelevant

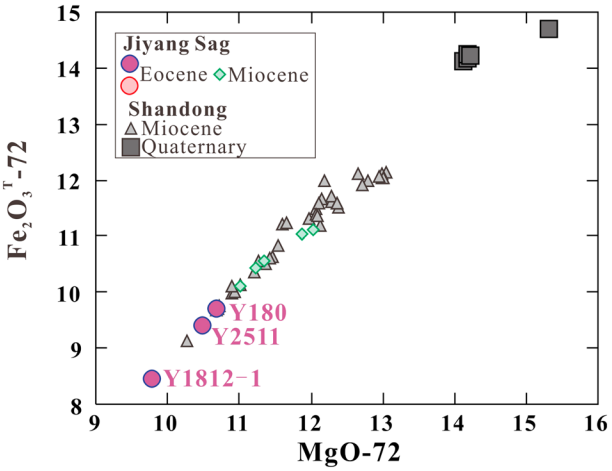

Figure 10. $Fe_2O_3^T$ (in wt %) versus MgO (in wt %) correlation for basalts from the Jiyang Sag and Shandong, after correction for fractionation effect to $Mg^{\#} = 72$ using liquid lines of descent derived from MORB [see *Niu and O'Hara*, 2008]. The data source of Shandong basalts is as that in Figure 4.

whether the source is peridotite [e.g., *Walter*, 1998] or garnet pyroxenite [e.g., *Kogiso et al*., 2003]. The observations above indicate that the Quaternary nephelinites reflect lower degree melting at greater mantle depths than do the Miocene tholeiites and alkali basalts.

6.2.3. Distinctive Geochemical Characteristics of Rifting-Stage Basalts in the Jiyang Sag

Apart from *Li et al*. [2014], there are comparatively few studies of the rifting-stage basalts in the NCC. The rift-related basalts in the Jiyang Sag plot between EMI and MORB in $^{87}Sr/^{86}Sr(t)$ versus $\varepsilon_{Nd}(t)$ space (Figure 8a) and define a trend similar to the postrifting basalts. However, the rifting-stage basalts have relatively higher ε_{Hf} values at $\varepsilon_{Nd} > 0$ than do the postrifting basalts (Figure 8b). In terms of major elements, the rifting-stage basalts have higher SiO_2 and Al_2O_3 and lower MgO and $Fe_2O_3^T$ than the postrifting-stage basalts at a given $Mg^{\#}$ (Figure 5).

Dy, Y, and Yb are incompatible in olivine and pyroxene in basaltic melting and crystallization, and their olivine/melt and pyroxene/melt partition coefficients $\left(D_{element}^{mineral/melts}\right)$ are comparably small [e.g., *McKenzie and O'Nions*, 1991; *Johnson*, 1998; *Pertermann et al*., 2004; *Dasgupta et al*., 2009]. However, $D_{element}^{garnet/melt}$ increases markedly from Dy to Y then to Yb [e.g., *McKenzie and O'Nions*, 1991; *Johnson*, 1998; *Pertermann et al*., 2004; *Dasgupta et al*., 2009]. Dy, Y, and Yb in basalts should therefore be able to distinguish the effects of melting a mantle source in which garnet is in the residue. The postrift basalts exhibit very slightly increasing Yb and constant Lu contents, while their Zr concentrations vary widely, from 112 to 359 ppm, with the low-SiO_2 basalts having higher Zr than high-SiO_2 basalts (Figures 7c and 7d). These features are consistent with the involvement of two mantle sources, both of which include residual garnet.

The Miocene tholeiites from Jiyang Sag have Dy/Yb ratios of 2.7 ~ 2.8 and Y/Yb ratios of 12.0 ~ 12.6, which are significantly lower than those of the Quaternary Dashan nephelinites (4.1 ~ 4.4 and 17.1 ~ 20.0, respectively, Figure 9), indicating a larger fraction of residual garnet in the Dashan nephelinite source (i.e., carbonated garnet pyroxenite + peridotite) as compared to the Jiyang Sag tholeiites (garnet pyroxenite). This is also consistent with the carbonated source of the nephelinites being deeper than the tholeiite source, as garnet stabilizes at higher pressures and is consumed more slowly during high-pressure melt generation [e.g., *Walter*, 1998; *Kogiso et al*., 2003].

The rifting-stage basalts show higher slopes of Yb and Lu versus Zr arrays compared to the postrift basalts, suggesting that there is less residual garnet in their mantle sources (Figures 7c and 7d). The rifting-stage basalts, with Dy/Yb of 2.1 ~ 2.7 and Y/Yb of 9.9 ~ 12.1, extend to lower values than do the postrift basalts. In Figure 11, the rifting-stage basalts form inverse Dy/Yb and Y/Yb versus $\varepsilon_{Hf}(t)$ correlations, whereas the postrifting-stage basalts form broad positive correlations. The rifting and postrifting basalts appear to share a similar mixing end-member, at $\varepsilon_{Hf}(t)$ of ~ 3.0 and Y/Yb of ~ 13.0. The rifting-stage basalts involve another mixing end-member that is similar to E-MORB.

The rifting and postrifting basalts have similar isotopically enriched components, both with an EMI-like signature (Figure 8a); high SiO_2 and Al_2O_3 but low MgO and $Fe_2O_3^T$ (Figure 5); and low Dy/Yb and Y/Yb ratios (Figure 11). However, their isotopically depleted components are different in terms of major and trace elements and radiogenic isotopes. The isotopically depleted components of the rifting-stage basalts have major elements similar to enriched MORB (Figure 5) and lower Dy/Yb and Y/Yb than the postrifting basalts (Figure 11), suggesting little residual garnet in its mantle source. As such, the isotopically depleted mixing

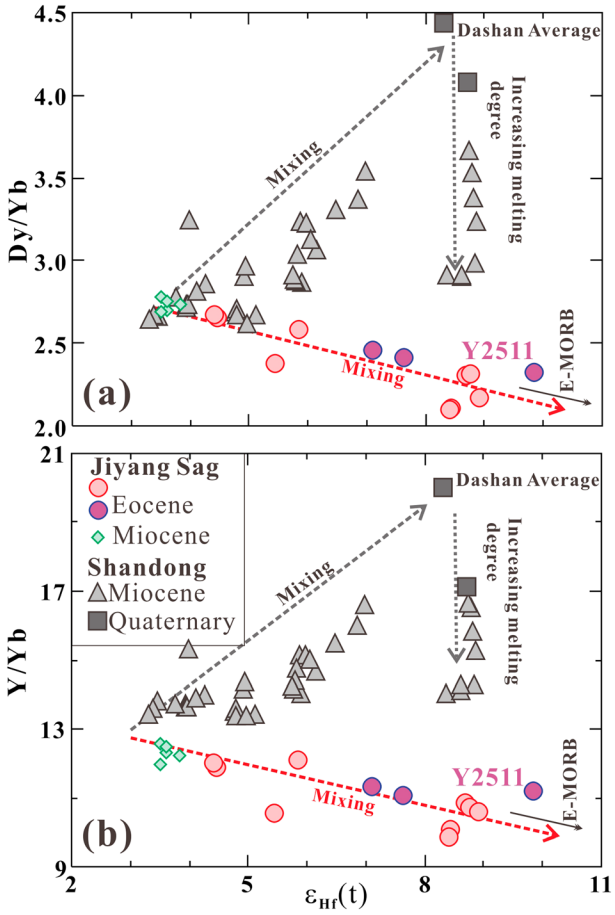

Figure 11. (a) Dy/Yb and (b) Y/Yb versus $\varepsilon_{Hf}(t)$ diagrams for basalts from the Jiyang Sag and Shandong. The data source of Shandong basalts is as that in Figure 8.

component for the rifting-stage basalts appears to be consistent with the low-pressure decompression melting of a peridotitic MORB source.

6.3. Heterogeneous Mantle Beneath Eastern NCC and Temporal Variation in Lithospheric Thickness

The geochronology and geochemistry of Cenozoic basalts in the eastern NCC shed light on the roles of lithospheric thickness [*Humphreys and Niu*, 2009; *Niu et al.*, 2011] and source effects [*Sobolev et al.*, 2005, 2007; *Herzberg*, 2006, 2011] on the geochemistry of intracontinental basalts. Seismic images reveal that the lithosphere beneath the Jiyang Sag is thinner than that beneath Shandong [*Chen*, 2010]. At ~ 23–20 Ma, basalts erupted in Jiyang Sag were tholeiitic (Figure 4a) with strong EMI signatures (Figure 8a), while the contemporaneous Shandong basalts, which have similar isotopic compositions, were alkalic [*Zeng et al.*, 2011]. This observation supports the idea that lithospheric thickness affected the depths and extents of melting of these EMI-influenced mantle sources.

In general, OIBs generated beneath thick mantle lithosphere have lower SiO_2 and higher $Fe_2O_3^T$ and TiO_2 than those generated under thin lithosphere [*Humphreys and Niu*, 2009; *Niu et al.*, 2011]. This is consistent with high-pressure experimental melting results on peridotite and garnet pyroxenite [e.g., *Walter*, 1998; *Kogiso et al.*, 2003] and indicates a lower degree of melting for basalt generated beneath thicker lithosphere. However, OIBs generated beneath thick lithosphere have less radiogenic $^{176}Hf/^{177}Hf$ and $^{143}Nd/^{144}Nd$ and more radiogenic $^{87}Sr/^{86}Sr$ and $^{206}Pb/^{204}Pb$ than those generated beneath thin lithosphere, indicating that lower degrees of melting are generally coupled with greater contributions from isotopically enriched components [*Humphreys and Niu*, 2009; *Niu et al.*, 2011]. The "OIB-like" basalt in the eastern NCC are geochemically different from typical OIB, e.g., the lower SiO_2 Dashan nephelinites (Figure 4) which have more radiogenic $^{176}Hf/^{177}Hf$ and $^{143}Nd/^{144}Nd$ than the other, higher SiO_2 basalts in Shandong (Figure 8b). Therefore, the geochemical compositions of these basalts are a function not only of lithospheric thickness but also of mantle source.

As discussed above, an enriched EMI mantle source was involved in the generation of basalts in the eastern NCC throughout the Cenozoic, but the isotopically depleted mantle source changed during rifting in the eastern NCC. The asthenospheric mantle beneath the eastern NCC is proposed to be composed of three components: (1) enriched, dispersed "plums" of garnet pyroxenite with an EMI radiogenic isotope signature; (2) a fertile peridotite matrix; and (3) a deeper carbonated eclogite source (Figure 12a). Recent work by *Thomson et al.* [2016] has found that the majority of slab geotherms intersect the solidi of carbonated oceanic crust at depths of approximately 300 to 700 km. Carbonatite melts generated from this carbonated eclogite within or near the MTZ have the ability to refertilize the overlying mantle and reduce its solidus [*Dasgupta et al.*, 2004; *Thomson et al.*, 2016]. These carbonatite melts would extract a substantial inventory of trace

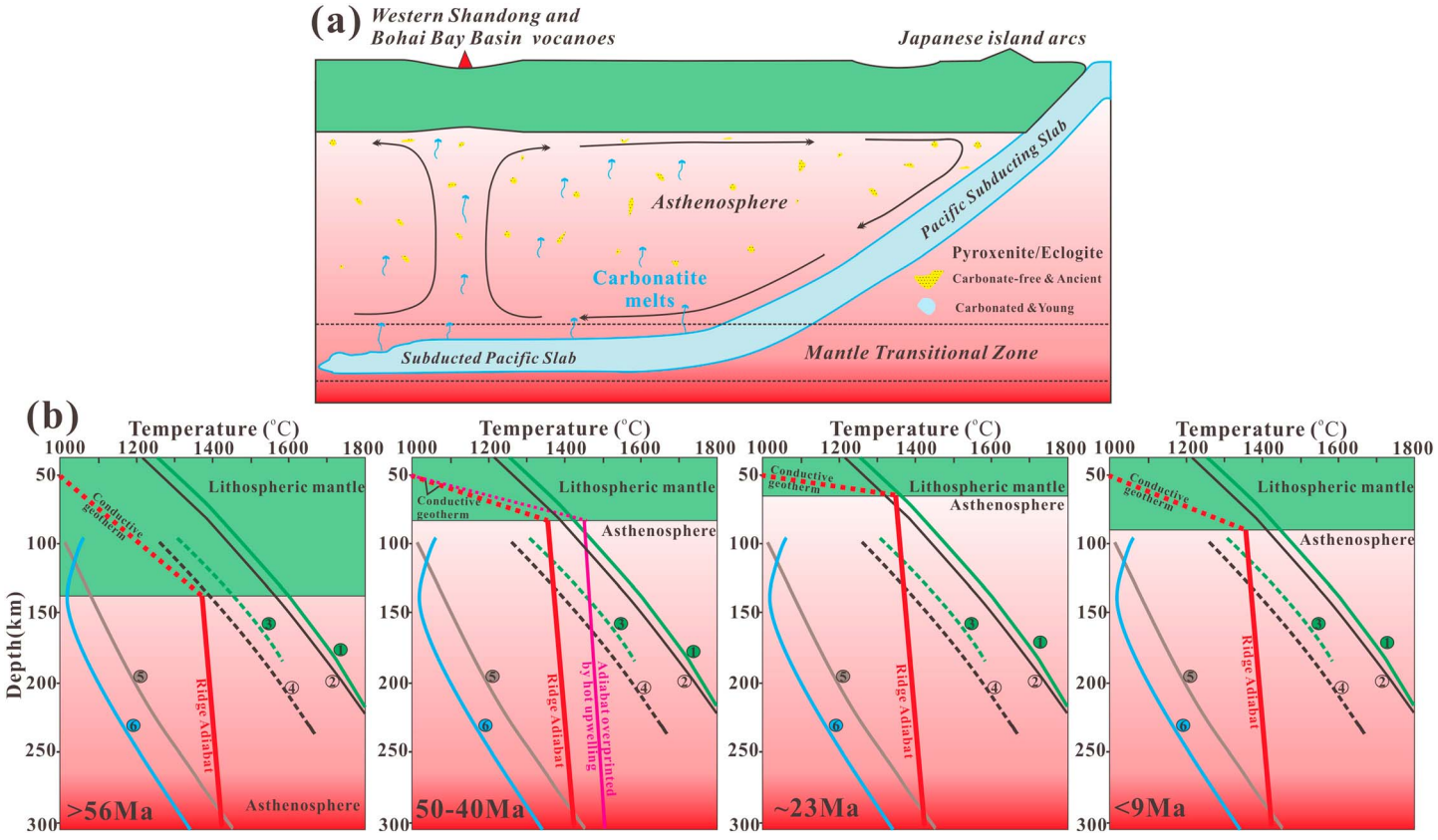

Figure 12. Cartoon illustrating mantle heterogeneity beneath the eastern NCC and lithospheric thickness variation inducing magma source shift. (a) Asthenospheric mantle beneath the eastern NCC, including dispersed zones of pyroxenite with EMI isotopic signature, is metasomatized by carbonatite melts/fluids from carbonated eclogite of the subducted Pacific slab in the mantle transition zone. (b) Variation of lithospheric thickness-induced changes in the lengths of mantle melting columns explains the temporal chemical evolution of the basaltic lavas. Mantle solidi: (1) peridotite [*Hirschmann*, 2000]; (2) garnet pyroxenite [*Kogiso et al*., 2003]; (3) carbonated silicate melting of peridotite [*Dasgupta et al*., 2007]; (4) carbonated silicate melting of garnet pyroxenite [*Dasgupta et al*., 2007]; (5) carbonated peridotite [*Dasgupta et al*., 2006]; and (6) carbonated eclogite [*Dasgupta et al*., 2004].

elements from the eclogite, based on trace element partitioning data between garnet lherzolite and carbonatite [*Dasgupta et al*., 2009]. In the case of the NCC, these carbonatite melts also carry the isotopic signature of the subducted Pacific slab. The asthenosphere beneath the eastern NCC is composed of fertile peridotite with dispersed domains of garnet pyroxenite, and carbonatite melts likely migrated into this mantle at shallower depths (<410 km) (Figure 12a). These carbonatite melts would metasomatize both garnet pyroxenite and peridotite in the shallower mantle and catalyze the generation of carbonated silicate melts [*Dasgupta et al*., 2007].

Castillo [2015, 2016] and *Weiss et al*. [2016] have both argued for the formation of the HIMU (high μ (μ = $^{238}U/^{204}Pb$)) mantle source based on a model of ancient carbonate recycling. In this study, we propose that carbonate veins in the basaltic oceanic crust are the source of the carbonatite. The oceanic crust is already dehydrated, and sediments are expected to be a minimal constituent before this crust is transported into the MTZ. Melting of this dehydrated oceanic crust in the presence of carbonate will produce the trace element patterns observed in the Dashan nephelinites [*Sakuyama et al*., 2013].

To account for the petrogenetic evolution of the BBB basalts, we propose a shift in the depths of magma sources over time in association with lithospheric thickness changes through the Cenozoic (Figure 12b). During Eocene rifting in the BBB (and lithospheric thinning of the NCC), decompression melting of the uppermost asthenosphere, comprising garnet pyroxenite domains dispersed within a fertile peridotite matrix, led to basaltic magmatism [*Li et al*., 2014]. Although partial melting of a carbonated garnet pyroxenite/peridotite mantle source could generate carbonated silicate melting, this melt production would be minor relative to that of fertile asthenospheric peridotite, so melts of this isotopically depleted peridotite were initially the

dominant component. The involvement of a MORB-like isotopically depleted component in forming the rift basalts is consistent with their convex ε_{Hf}-ε_{Nd} correlation trend (Figure 8b). Inputs of melts from a depleted mantle source with little garnet in the uppermost asthenospheric mantle are consistent with the geochemistry of the BBB rift basalts.

Progressive lithospheric thinning in the NCC up until 23–20 Ma would serve to raise the asthenospheric mantle above the solidus of garnet pyroxenite (≤70 km) [*Kogiso et al*., 2003]. However, as there is no evidence for vigorous extension and associated upwelling after 23 Ma in the eastern NCC, decompression melting of fertile peridotite in the uppermost asthenosphere is unlikely. The relative contribution from carbonated mantle sources would thus increase and became more evident under these conditions. Garnet pyroxenite melting generated the tholeiites and alkali basalts in the BBB and Shandong, respectively, all of which exhibit strong EMI signatures. These melts mixed with carbonated silicate melts responsible for the generation of the basanites. A thickened lithosphere resulting from thermal decay at < 9 Ma [*Xu*, 2001; *Xu et al*., 2009; *Li et al*., 2016a] discouraged melting of garnet pyroxenite, as the mantle adiabat no longer crossed its solidus, though the solidi of carbonated mantle sources could be crossed. Melting of garnet pyroxenite and peridotite that had been metasomatized by deep-derived carbonatite melts produced nephelinite magmas at 130–110 km (initial depth). As carbonatite melts retain the isotopic signature of the subducted Pacific slab, the postrifting basalts form a concave mixing trend in ε_{Hf}-ε_{Nd} space (Figure 8b).

6.4. Geochronological and Geochemical Perspectives on the *P* Wave Tomography of the Mantle Beneath the Eastern NCC

As noted earlier, the mantle beneath the eastern NCC is more structurally and compositionally complicated than that beneath typical hot spots. The subducted Pacific slab in the mantle transition zone (MTZ) is generally believed to have contributed to the heterogeneity of the mantle beneath the eastern NCC [e.g., *Zhu et al*., 2012] although the specifics of those contributions are a source of debate. The idea that the EMI signatures of basaltic lavas in northeastern China are related to wet upwelling from the MTZ, triggered by dehydration of the stagnant Pacific slab in the MTZ [e.g., *Zhao et al*., 2009; *Kuritani et al*., 2011; *Liu et al*., 2015], is inconsistent with several lines of evidence: (1) Low-velocity mantle domains exist both above the stagnant Pacific slab and westward to the leading edge of the currently subducting Pacific plate [*Li and van der Hilst*, 2010; *Zhao*, 2012; *Lei*, 2012]. These observations indicate that the occurrence of low-velocity mantle domains may not be exclusively linked to dehydration of the Pacific plate. (2) For the postrifting basalts in this study, the samples with the strongest EMI isotopic signatures were those derived from shallower garnet pyroxenitic mantle sources, while the more isotopically depleted basalts (e.g., the Dashan nephelinites) were derived from deeper, carbonated mantle sources [*Zeng et al*., 2010; *Sakuyama et al*., 2013; *Li et al*., 2016a]. (3) The rifting-stage basalts in the BBB also preserve an EMI signature (Figure 8), and this signature shows mixing relationships with an isotopically depleted signature from shallower, fertile peridotite mantle sources, similar to that of MORB but clearly distinct from that of the Dashan nephelinite (Figures 5, 8, and 11). (4) Recent work on the water contents of Shandong basalts reveal that the shallower EMI mantle-derived basalts have higher H_2O/Ce than the deeper-derived basalts [*Liu et al*., 2015]. As such, the EMI signature evident in NCC basalts is probably not related to the wet upwelling of the MTZ. As noted above, EMI mantle domains are more likely to persist as pyroxenitic horizons dispersed in the asthenosphere beneath the eastern NCC. Such enriched "blobs" are proposed to be ubiquitous beneath both continental and oceanic lithosphere [*Fitton*, 2007].

The Hf-Nd isotopic composition of the Dashan nephelinites (<1 Ma) in particular shows strong affinities with that of the Pacific mantle domain (Figure 8b), suggesting that the nephelinite source may have included inputs from the Pacific slab, possibly via additions from carbonatite melts [e.g., *Li et al*., 2016a]. The subducted Pacific slab geotherm will intersect the solidi of carbonated oceanic crust in the MTZ [*Thomson et al*., 2016]. Carbonatite melts would, given their low density, migrate upward into the upper mantle. As the carbonatite will freeze to become diamond if the oxygen fugacity of ambient peridotitic mantle is reducing [*Rohrbach and Schmidt*, 2011], the prerequisite for these carbonatite melts migrating into the shallower upper mantle is the existence of garnet pyroxenite/eclogite at depths of < 410 km as these enriched mantle domains contain recycled materials [*Li et al*., 2014; *Liu et al*., 2015] and thus may be oxidized than the peridotitic mantle.

Based on our combined geochemical evidence, the low *P* wave velocity domain imaged beneath the NCC in seismic tomographic studies represents preexisting heterogeneous mantle that has been modified by later, slab-derived carbonatite melts/fluids. The preexisting pyroxenitic mantle domains may be acting both as

conduits and "sponges" for these metasomatizing liquids, and it is these metasomatizing agents that encourage the melting of these domains under appropriate mantle *P-T* conditions. So the prominent low-velocity mantle column observed beneath the Changbaishan volcano is more likely to reflect a mineralogical/petrologic anomaly, i.e., more preexisting metasomatized garnet pyroxenite/eclogite at depth, as opposed to a "hot" or "wet" mantle column, as has been proposed for many hot spots as well as the NCC [e.g., *Lei and Zhao*, 2006; *Huang and Zhao*, 2006; *Zhao et al*., 2009; *Wei et al*., 2015; *French and Romanowicz*, 2015]. Another characteristic of the MTZ beneath the eastern Eurasia is its high electrical conductivity at depths between 410 and 670 km [*Kelbert et al*., 2009]. On the basis of laboratory measurements, *Gaillard et al*. [2008] found that that molten carbonates have electrical conductivities that are 3 orders of magnitude higher than those of molten silicate and 5 orders of magnitude higher than those of hydrated olivine. Therefore, the presence of small amounts of carbonate melt in the MTZ beneath the eastern Eurasia provides a plausible explanation for its high electrical conductivity.

The evolutionary pattern of NCC magmatism (tholeiites to alkali basalts to nephelinites) parallels what is seen over time in Hawaiian volcanoes [e.g., *McDonald and Katsura*, 1964] albeit over a longer time span. Geochemically, the Hawaiian shield volcanoes (e.g., Kilauea, Mauna Loa, and Koolau) show elemental and isotopic compositions strongly correlated with their SiO_2 abundances, with the higher SiO_2 samples having higher Ba/Th and lower Ce/Pb ratios and strong EMI isotopic compositions [*Tanaka and Nakamura*, 2005]. A similar situation is also observed for the NCC basalts (see discussion above). These observations may speak to similarities in their mantle mineralogies and may indicate broadly similar trajectories in the evolution of mantle melting in both localities, irrespective of differences in their isotopic sources.

7. Conclusions

Clear differences are evident in the chemistries of basalts erupted during (56–23 Ma) and after rifting (≤23 Ma) of the Bohai Bay Basin (BBB) region of the eastern NCC. These two episodes of basalts reflect the mixing of isotopically depleted sources and an EMI mantle source. While the postrifting basalts include an isotopically depleted component that is consistent with a deep, carbonated mantle source (garnet pyroxenite + peridotite), the isotopically depleted components in the rifting-stage basalts are geochemically constrained to be derived from a shallower fertile peridotite source with little residual garnet. Geochronological and geochemical results for the Cenozoic basalts from the BBB indicate that the asthenospheric mantle beneath the eastern NCC is vertically heterogeneous with respect to its chemistry and phase assemblages. Garnet pyroxenites with EMI radiogenic isotope signatures are dispersed in fertile peridotite, while a carbonated eclogite source that preserved the isotopic signature of the Pacific mantle domain existed at greater depths. Carbonatite melts formed from this carbonated eclogite reservoir further modified the mantle and produced further isotopic and compositional heterogeneity beneath the eastern NCC. The tapping of these magma sources was controlled by lithospheric evolution: during lithospheric thinning of the eastern NCC, the rifting-stage basalts of the BBB were generated via decompression melting of the uppermost asthenosphere, which included garnet pyroxenite dispersed in fertile peridotite. After lithospheric thinning in the eastern NCC, basalts were derived via partial melting of a mantle source that included garnet pyroxenites at shallow depths and a carbonated source from greater depths. The low-velocity mantle domains identified beneath the eastern NCC by recent seismic tomography are closely related to melting of carbonated eclogite in the deep mantle.

Acknowledgments

The data supporting this paper are available as supporting information. We thank Jinlong Ma and Le Zhang for analytical assistance in bulk rock Sr-Nd-Hf isotopes and Huaning Qiu for bulk rock ^{40}Ar-^{39}Ar dating. We gratefully acknowledge Pat Castillo and one anonymous reviewer for their constructive and thoughtful comments that helped improve the manuscript. Editorial handling by Michael Walter is greatly appreciated. Our research was supported by the Strategic Priority Research Program of the Chinese Academy of Sciences (grant XDB18000000) and by the National Natural Science Foundation of China (NSFC projects 41688103, 41472210 and 41273042). This is contribution IS-2329 to GIG-CAS.

References

Allen, M. B., D. I. M. Macdonald, X. Zhao, S. J. Vincent, and C. Brouet-Menzies (1997), Early Cenozoic two-phase extension and late Cenozoic thermal subsidence and inversion of the Bohai Basin, North China, *Mar. Petrol. Geol.*, *14*, 951–972.

Blichert-Toft, J., and F. Albarède (1997), The Lu-Hf isotope geochemistry of chondrites and the evolution of the mantle-crust system, *Earth Planet. Sci. Lett.*, *148*(1–2), 243–258.

Castillo, P. R. (2015), The recycling of marine carbonates and sources of HIMU and FOZO ocean island basalts, *Lithos*, *216–217*, 254–263.

Castillo, P. R. (2016), A proposed new approach and unified solution to old Pb paradoxes, *Lithos*, *252–253*, 32–40.

Chen, L. (2010), Concordant structural variations from the surface to the base of the upper mantle in the North China Craton and its tectonic implications, *Lithos*, *120*, 96–115.

Chen, L. H., G. Zeng, S. Y. Jiang, A. W. Hofmann, X. S. Xu, and M. B. Pan (2009), Sources of Anfengshan basalts: Subducted lower crust in the Sulu UHP belt, China, *Earth Planet. Sci. Lett.*, *286*, 426–435.

Chu, Z. Y., F. Y. Wu, R. J. Walker, R. L. Rudnick, L. Pitcher, I. S. Puchtel, Y. H. Yang, and S. A. Wilde (2009), Temporal evolution of the lithospheric mantle beneath the eastern North China Craton, *J. Petrol.*, *50*, 507–529.

Dasgupta, R., M. M. Hirschmann, and A. C. Withers (2004), Deep global cycling of carbon constrained by the solidus of anhydrous, carbonated eclogite under upper mantle conditions, *Earth Planet. Sci. Lett.*, *227*, 73–85.

Dasgupta, R., M. M. Hirschmann, and K. Stalker (2006), Immiscible transition from carbonate rich to silicate-rich melts in the 3 GPa melting interval of eclogite plus CO_2 and genesis of silica-undersaturated ocean island lavas, *J. Petrol.*, *47*, 647–671.
Dasgupta, R., M. M. Hirschmann, and N. D. Smith (2007), Partial melting experiments of peridotite CO_2 at 3 GPa and genesis of alkalic ocean island basalts, *J. Petrol.*, *48*, 2093–2124.
Dasgupta, R., M. M. Hirschmann, W. F. McDonough, M. Spiegelman, and A. C. Withers (2009), Trace element partitioning between garnet lherzolite and carbonatite at 6.6 and 8.6 GPa with applications to the geochemistry of the mantle and of mantle-derived melts, *Chem. Geol.*, *262*, 57–77.
Fan, Q. C., and P. R. Hooper (1991), The Cenozoic basaltic rocks of eastern China: Petrology and chemical composition, *J. Petrol.*, *32*, 765–810.
Fitton, J. G. (2007), *The OIB Paradox*, *Special Paper*, vol. 430, pp. 387–412, Geological Society, America.
French, S. W., and B. Romanowicz (2015), Broad plumes rooted at the base of the Earth's mantle beneath major hotspots, *Nature*, *525*, 95–99.
Fukao, Y., M. Obayashi, H. Inoue, and M. Nenbai (1992), Subducting slab stagnant in the mantle transition zone, *J. Geophys. Res.*, *97*, 4809–4822, doi:10.1029/91JB02749.
Gaillard, F., M. Malki, G. Iacono-Marziano, M. Pichavant, and B. Scaillet (2008), Carbonatite melts and electrical conductivity in the asthenosphere, *Science*, *322*, 1363–1365.
Gale, A., C. A. Dalton, C. H. Langmuir, Y. J. Su, and J. G. Schilling (2013), The mean composition of ocean ridge basalts, *Geochem. Geophys. Geosyst.*, *14*, 489–518, doi:10.1029/2012GC004334.
Griffin, W. L., O'Reilly, S. Y., Ryan, C. G. (1992), Composition and thermal structure of the lithosphere beneath South Africa, Siberia and China: Proton microprobe studies, Abstr. of the Int. Symp. on Cenozoic Volcanic Rocks and Deep-seated Xenoliths of China and its Environ., pp. 65–66, Beijing.
Griffin, W. L., A. D. Zhang, S. Y. O'Reilly, and C. G. Ryan (1998), Phanerozoic evolution of the lithosphere beneath the Sino-Korean craton, in *Mantle Dynamics and Plate Interactions in East Asia*, *Geodyn. Ser.*, vol. 27, edited by M. F. J. Flower et al., pp. 107–126, AGU, Washington, D. C.
Gurenko, A. A., A. V. Sobolev, K. A. Hoernle, F. Hauff, and H. U. Schmincke (2009), Enriched, HIMU-type peridotite and depleted recycled pyroxenite in the Canary plume: A mixed-up mantle, *Earth Planet. Sci. Lett.*, *277*, 514–524.
Harnois, L. (1988), The CIW index: A new chemical index of weathering, *Sediment. Geol.*, *55*, 319–322.
He, H. Y., C. L. Deng, Y. X. Pan, T. Deng, Z. H. Luo, J. M. Sun, and R. X. Zhu (2011), New $^{40}Ar/^{39}Ar$ dating results from the Shanwang Basin, eastern China: Constraints on the age of the Shanwang Formation and associated biota, *Phys. Earth Planet. Int.*, *187*, 66–75.
He, L. J. (2015), Thermal regime of the North China Craton: Implications for craton destruction, *Earth Sci. Rev.*, *140*, 14–26.
Herzberg, C. (2006), Petrology and thermal structure of the Hawaiian plume from Mauna Kea volcano, *Nature*, *444*, 605–609.
Herzberg, C. (2011), Identification of source lithology in the Hawaiian and Canary Islands: Implications for origins, *J. Petrol.*, *52*, 113–146.
Hirschmann, M. M. (2000), The mantle solidus: Experimental constraints and the effect of peridotite composition, *Geochem. Geophys. Geosyst.*, *1*, 1042, doi:10.1029/2000GC000070.
Hirschmann, M. M., T. Kogiso, M. B. Baker, and E. M. Stolper (2003), Alkalic magmas generated by partial melting of garnet pyroxenite, *Geology*, *31*, 481–484.
Hu, S. B., P. B. O'Sullivan, A. Raza, and B. P. Kohn (2001), Thermal history and tectonic subsidence of the Bohai Basin, northern China: A Cenozoic rifted and local pull-apart basin, *Phys. Earth Planet. Int.*, *126*, 221–235.
Huang, J. L., and D. P. Zhao (2006), High-resolution mantle tomography of China and surrounding regions, *J. Geophys. Res.*, *111*, B09305, doi:10.1029/2005JB004066.
Huang, J., S. G. Li, Y. L. Xiao, S. Ke, W. Y. Li, and Y. Tian (2015), Origin of low $\delta^{26}Mg$ Cenozoic basalts from South China Block and their geodynamic implications, *Geochim. Cosmochim. Acta*, *164*, 298–317.
Humphreys, E. R., and Y. L. Niu (2009), On the composition of ocean island basalts (OIB): The effects of lithospheric thickness variation and mantle metasomatism, *Lithos*, *112*, 118–136.
Jacobsen, S. B., and G. J. Wasserburg (1980), Sm-Nd isotopic evolution of chondrites, *Earth Planet. Sci. Lett.*, *50*(1), 139–155.
Johnson, K. T. M. (1998), Experimental determination of partition coefficients for rare earth and high-field-strength elements between clinopyroxene, garnet, and basaltic melt at high pressures, *Contrib. Mineral. Petrol.*, *133*, 60–68.
Kelbert, A., A. Schultz, and G. Egbert (2009), Global electromagnetic induction constraints on transition-zone water content variations, *Nature*, *460*, 1003–1006.
Kogiso, T., K. Hirose, and E. Takahashi (1998), Melting experiments on homogeneous mixtures of peridotite and basalt: Application to the genesis of ocean island basalts, *Earth Planet. Sci. Lett.*, *162*, 45–61.
Kogiso, T., M. M. Hirschmann, and D. J. Frost (2003), High-pressure partial melting of garnet pyroxenite: Possible mafic lithologies in the source of ocean island basalts, *Earth Planet. Sci. Lett.*, *216*, 603–617.
Koppers, A. A. P. (2002), ArArCALC—Software for $^{40}Ar/^{39}Ar$ age calculations, *Comput. Geosci.*, *28*, 605–619.
Kuritani, T., E. Ohtani, and J. I. Kimura (2011), Intensive hydration of the mantle transition zone beneath China caused by slab stagnation, *Nat. Geosci.*, *4*, 713–716.
Le Bas, M. J., R. W. Le Maitre, A. Strekeisen, and B. Zanettin (1986), A chemical classification of volcanic rocks based on the total alkali–silica diagram, *J. Petrol.*, *27*, 745–750.
Lei, J. S. (2012), Upper-mantle tomography and dynamics beneath the North China Craton, *J. Geophys. Res.*, *117*, B06313, doi:10.1029/2012JB009212.
Lei, J. S., and D. P. Zhao (2006), A new insight into the Hawaiian plume, *Earth Planet. Sci. Lett.*, *241*, 438–453.
Li, C., and R. D. van der Hilst (2010), Structure of the upper mantle and transition zone beneath Southeast Asia from traveltime tomography, *J. Geophys. Res.*, *115*, B07308, doi:10.1029/2009JB006882.
Li, H. Y., X. L. Huang, and H. Guo (2014), Geochemistry of Cenozoic basalts from the Bohai Bay Basin: Implications for a heterogeneous mantle source and lithospheric evolution beneath the eastern North China Craton, *Lithos*, *196–197*, 54–66.
Li, H. Y., Y. G. Xu, J. G. Ryan, X. L. Huang, Z. Y. Ren, H. Guo, and Z. G. Ning (2016a), Olivine and melt inclusion chemical constraints on the source of intracontinental basalts from the eastern North China Craton: Discrimination of contributions from the subducted Pacific slab, *Geochim. Cosmochim. Acta*, *178*, 1–19.
Li, H. Y., Z. Zhou, J. G. Ryan, G. J. Wei, and Y. G. Xu (2016b), Boron isotopes reveal multiple metasomatic events in the mantle beneath the eastern North China Craton, *Geochim. Cosmochim. Acta*, *194*, 77–90.
Li, X. H., C. S. Qi, Y. Liu, X. R. Liang, X. L. Tu, L. W. Xie, and Y. H. Yang (2005), Petrogenesis of the Neoproterozoic bimodal volcanic rocks along the western margin of the Yangtze Block: New constraints from Hf isotopes and Fe/Mn ratios, *Chin. Sci. Bull.*, *50*, 2481–2486.
Liu, D. Y., A. P. Nutman, W. Compston, J. S. Wu, and Q. H. Shen (1992), Remnants of ≥3800 Ma crust in the Chinese part of the Sino-Korean Craton, *Geology*, *20*, 339–342.

Liu, J., Q. K. Xia, E. Deloule, H. Chen, and M. Feng (2015), Recycled oceanic crust and marine sediment in the source of alkali basalts in Shandong, eastern China: Evidence from magma water content and oxygen isotopes, *J. Geophys. Res. Solid Earth*, *120*, 8281–8303, doi:10.1002/2015JB012476.
McDonald, G. A., and T. Katsura (1964), Chemical composition of Hawaiian lavas, *J. Petrol.*, *5*, 82–133.
McDonough, W. F., and S. S. Sun (1995), The composition of the Earth, *Chem. Geol.*, *120*, 223–253.
McKenzie, D. P., and R. K. O'Nions (1991), Partial melt distributions from inversion of rare earth element concentrations, *J. Petrol.*, *32*, 1021–1091.
Menzies, M. A., and Y. G. Xu (1998), Geodynamics of the North China Craton, in *Mantle Dynamics and Plate Interactions in East Asia*, *Geodynamics Series*, vol. 27, edited by M. Flower et al., pp. 155–165, AGU, Washiongton, D. C.
Menzies, M. A., W. M. Fan, and M. Zhang (1993), Palaeozoic and Cenozoic lithoprobes and the loss of >120 km of Archaean lithosphere, Sino-Korean craton, China, *Geol. Soc. London, Spec. Publ.*, *76*(1), 71–81, doi:10.1144/GSL.SP.1993.076.01.04.
Meschede, M. (1986), A method of discriminating between different types of mid-ocean ridge basalts and continental tholeiites with the Nb–Zr–Y diagram, *Chem. Geol.*, *56*, 207–218.
Niu, Y. L., and M. J. O'Hara (2003), Origin of ocean island basalts: A new perspective from petrology, geochemistry, and mineral physics considerations, *J. Geophys. Res.*, *108*(B4), 2209.
Niu, Y. L., and M. J. O'Hara (2008), Global correlations of ocean ridge basalt chemistry with axial depth: A new perspective, *J. Petrol.*, *49*, 633–664.
Niu, Y. L., M. Wilson, E. R. Humphreys, and M. J. O'Hara (2011), The origin of intra-plate ocean island basalts (OIB): The lid effect and its geodynamic implications, *J. Petrol.*, *52*, 1443–1468.
Parsons, B., and J. G. Sclater (1977), An analysis of the variation of ocean floor bathymetry and heat flow with age, *J. Geophys. Res.*, *82*, 803–827, doi:10.1029/JB082i005p00803.
Pearce, J. A., P. D. Kempton, G. M. Nowell, and S. R. Noble (1999), Hf-Nd element and isotope perspective on the nature and provenance of mantle and subduction components in western Pacific arc-basin systems, *J. Petrol.*, *40*(11), 1579–1611.
Pertermann, M., M. M. Hirschmann, K. Hametner, D. Günther, and M. W. Schmidt (2004), Experimental determination of trace element partitioning between garnet and silica-rich liquid during anhydrous partial melting of MORB-like eclogite, *Geochem. Geophys. Geosyst.*, *5*, Q05A01, doi:10.1029/2003GC000638.
Phipps Morgan, J., and W. F. S. Smith (1992), Flattening of the sea-floor depth-age curve as a response to asthenospheric flow, *Nature*, *359*, 524–527.
Qi, J. F., and Q. Yang (2010), Cenozoic structural deformation and dynamic processes of the Bohai Bay basin province, China, *Mar. Petrol. Geol.*, *27*, 757–771.
Qin, X. F. (2008), Geochronology and geochemistry of the Tertiary basalts from the Midanjiang-Mishan regions: Mantle source characteristics and its spatial-temporal evolution, PhD dissertation, 125 pp., Graduate School of Chinese Academy of Sciences, Beijing.
Qiu, H. N., and Y. D. Jiang (2007), Sphalerite $^{40}Ar/^{39}Ar$ progressive crushing and stepwiseheating techniques, *Earth Planet. Sci. Lett.*, *256*, 224–232.
Rohrbach, A., and M. W. Schmidt (2011), Redox freezing and melting in the Earth's deep mantle resulting from carbon–iron redox coupling, *Nature*, *472*, 209–212.
Rudnick, R. L., and S. Gao (2003), Composition of the Continental Crust, in *The Crust: Treatise on Geochemistry*, vol. 3, edited by H. D. Holland and K. K. Turekian, pp. 1–64, Elsevier-Pergamon, Oxford.
Sakuyama, T., et al. (2013), Melting of dehydrated oceanic crust from the stagnant slab and of the hydrated mantle transition zone: Constraints from Cenozoic alkaline basalts in eastern China, *Chem. Geol.*, *359*, 32–48.
Sobolev, A. V., A. W. Hofmann, S. V. Sobolev, and I. K. Nikogosian (2005), An olivine-free mantle source of Hawaiian shield basalts, *Nature*, *434*, 590–597.
Sobolev, A. V., et al. (2007), The amount of recycled crust in source of mantle-derived melts, *Nature*, *316*, 412–417.
Stein, C. A., and S. Stein (1992), A model for the global variation in oceanic depth and heatflow with lithospheric age, *Nature*, *359*, 123–129.
Su, Y., and Langmuir, C. H. (2003), Global MORB chemistry compilation at the segment scale, PhD Thesis, Department of Earth and Environmental Sciences, Columbia University. [Available at http://petdb.ldeo.columbia.edu/documentation/morbcompilation/.]
Sun, S. S., and W. F. McDonough (1989), Chemical and isotopic systematics of oceanic basalts: Implications for mantle composition and processes, in *Magmatism in the Ocean Basins*, *Special Publication*, vol. 42, edited by A. D. Saunders and M. J. Norry, pp. 313–345, Geol. Soc., London.
Tanaka, R., and E. Nakamura (2005), Boron isotopic constraints on the source of Hawaiian shield lavas, *Geochim. Cosmochim. Acta*, *69*(13), 3385–3399.
Tang, Y. C., M. Obayashi, F. L. Niu, S. P. Grand, Y. J. Chen, H. Kawakatsu, S. Tanaka, J. Y. Ning, and J. F. Ni (2014), Changbaishan volcanism in northeast China linked to subduction-induced mantle upwelling, *Nat. Geosci.*, *7*, 470–474.
Thomson, A. R., M. J. Walter, S. C. Kohn, and R. A. Brooker (2016), Slab melting as a barrier to deep carbon subduction, *Nature*, *529*, 76–79.
Walter, M. J. (1998), Melting of garnet peridotite and the origin of komatiite and depleted lithosphere, *J. Petrol.*, *39*, 29–60.
Wei, W., D. Zhao, J. Xu, F. Wei, and G. Liu (2015), P and S wave tomography and anisotropy in northwest Pacific and east Asia: Constraints on stagnant slab and intraplate volcanism, *J. Geophys. Res. Solid Earth*, *120*, 1642–1666, doi:10.1002/2014JB011254.
Weis, D., B. Kieffer, C. Maerschalk, W. Pretorius, and J. Barling (2005), High-precision Pb-Sr-Nd-Hf isotopic characterization of USGS BHVO-1 and BHVO-2 reference materials, *Geochem. Geophys. Geosyst.*, *6*, Q02002, doi:10.1029/2004GC000852.
Weiss, Y., C. Class, S. L. Goldstein, and T. Hanyu (2016), Key new pieces of the HIMU puzzle from olivines and diamond inclusions, *Nature*, *537*, 666–670.
Workman, R. K., and S. R. Hart (2005), Major and trace element composition of the depleted MORB mantle (DMM), *Earth Planet. Sci. Lett.*, *231*, 53–72.
Wu, C. Z., L. X. Gu, Z. W. Ren, Z. Z. Zhang, Z. Y. Chen, and M. Zhao (2005), Transition from platemargin to intraplate environment: Geochemistry of basalts in Paleogene Liaohe basin, northeastern China, *Sci. China Ser. D Earth Sci.*, *48*(12), 2069–2080.
Wu, F. Y., Y. G. Xu, S. Gao, and J. P. Zheng (2008), Controversial on studies of the lithospheric thinning and craton destruction of North China, *Acta Petrol. Sin.*, *24*, 1145–1174.
Xia, Q. K., Y. T. Hao, P. Li, E. Deloule, M. Coltorti, L. Dallai, X. Z. Yang, and M. Feng (2010), Low water content of the Cenozoic lithospheric mantle beneath the eastern part of the North China Craton, *J. Geophys. Res.*, *115*, B07207, doi:10.1029/2009JB006694.
Xia, Q. K., J. Liu, S. C. Liu, I. Kova'cs, M. Feng, and L. Dang (2013), High water content in Mesozoic primitive basalts of the North China Craton and implications for the destruction of cratonic mantle lithosphere, *Earth Planet. Sci. Lett.*, *361*, 85–97.
Xu, Y. G. (2001), Thermo-tectonic destruction of the Archean lithospheric keel beneath eastern China: Evidence, timing and mechanism, *Phys. Chem. Earth*, *26*, 747–757.

Xu, Y. G., S. L. Chung, J. L. Ma, and L. B. Shi (2004), Contrasting Cenozoic lithospheric evolution and architecture in the Western and Eastern Sino-Korean Craton: Constraints from geochemistry of basalts and mantle xenoliths, *J. Geol.*, *112*, 593–605.

Xu, Y. G., H. Y. Li, C. J. Pang, and B. He (2009), On the time and duration of the destruction of the North China Craton, *Chin. Sci. Bull.*, *54*, 3379–3396.

Xu, Y. G., H. H. Zhang, H. N. Qiu, W. C. Ge, and F. Y. Wu (2012a), Oceanic crust components in continental basalts from Shuangliao, Northeast China: Derived from the mantle transition zone? *Chem. Geol.*, *328*, 168–184.

Xu, Z., Z. F. Zhao, and Y. F. Zheng (2012b), Slab–mantle interaction for thinning of cratonic lithospheric mantle in North China: Geochemical evidence from Cenozoic continental basalts in central Shandong, *Lithos*, *146*, 202–217.

Yang, W., F. Z. Teng, H. F. Zhang, and S. G. Li (2012), Magnesium isotopic systematics of continental basalts from the North China craton: Implications for tracing subducted carbonate in the mantle, *Chem. Geol.*, *328*, 185–194.

Zeng, G., L. H. Chen, X. S. Xu, S. Y. Jiang, and A. W. Hofmann (2010), Carbonated mantle sources for Cenozoic intra-plate alkaline basalts in Shandong, North China, *Chem. Geol.*, *273*, 35–45.

Zeng, G., L. H. Chen, A. W. Hofmann, and X. S. Xu (2011), Crust recycling in the sources of two parallel volcanic chains in Shandong, North China, *Earth Planet. Sci. Lett.*, *302*, 359–368.

Zhao, D. P. (2004), Global tomographic images of mantle plumes and subducting slabs: Insight into deep Earth dynamics, *Phys. Earth Planet. Int.*, *146*, 3–34.

Zhao, D. P. (2012), Tomography and dynamics of western-Pacific subduction zones, *Monogr. Environ. Earth Planets*, *1*(1), 1–70.

Zhao, D. P., Y. Tian, J. S. Lei, L. C. Liu, and S. H. Zheng (2009), Seismic image and origin of the Changbai intraplate volcano in East Asia: Role of big mantle wedge above the stagnant Pacific slab, *Phys. Earth Planet. Int.*, *173*, 197–206.

Zhou, X. H., and R. L. Armstrong (1982), Cenozoic volcanic rocks of eastern China—Secular and geographic trends in chemistry and strontium isotopic composition, *Earth Planet. Sci. Lett.*, *59*, 301–329.

Zhu, R. X., Y. G. Xu, G. Zhu, H. F. Zhang, Q. K. Xia, and T. Y. Zheng (2012), Destruction of the North China Craton, *Sci. China Earth Sci.*, *55*, 1565–1587.

Ziegler, P. A., and S. Cloetingh (2004), Dynamic processes controlling evolution of rifted basins, *Earth Sci. Rev.*, *64*, 1–50.

Zindler, A., and S. Hart (1986), Chemical geodynamics, *Ann. Rev. Earth Planet. Sci.*, *14*, 493–571.